Article

SOURCE DATA | TRANSPARENT PROCESS | OPEN ACCESS | CHECK FOR UPDATES

THE EMBO JOURNAL

Structural insights into bacterial dimethylsulfoniopropionate import by BCCT-family transporters

Yu-Zhong Zhang[1,2,3,10]✉, Wen-Jing Zhu[1,2,3,10], Kang Li[1,3,10], Hai-Tao Ding[4], Motoyuki Hattori[5], Shuaimeng Liu[5], Chang Ge[2], Qi-Long Qin[2,3], Zhao-Jie Teng[2], Ning-Hua Liu[2], Hai-Yan Cao[1,3], Chun-Yang Li[1,3], Xiu-Lan Chen[2,3], Qing-Tao Shen[6], Jonathan D Todd[1,7,8], Lu-Ning Liu[1,9]✉ & Peng Wang[1,3]✉

Abstract

Dimethylsulfoniopropionate (DMSP) is a ubiquitous marine organosulfur compound central to microbial stress responses, chemotaxis, and nutrient cycling. Its catabolism produces dimethylsulfide (DMS), a climate-active gas, and plays a key role in the global sulfur cycle. However, the molecular basis of DMSP import, underpinning its microbial metabolism, remains poorly understood. Here, we identify and characterize the BCCT-family transporter DddT from *Psychrobacter* sp. D2, a marine gamma-proteobacterium that utilizes DMSP as a carbon source. DddT is essential for DMSP uptake and functions as a Na^+-coupled symporter driven by the transmembrane sodium gradient. Using cryo-electron microscopy, we determined DddT structures in multiple conformational states, revealing its Na^+-dependent transport mechanism involving two sodium ions, one coordinated by a previously uncharacterized binding site. Sequence analysis shows that DddT-like proteins with conserved sodium-binding features are widespread in marine bacteria, suggesting this Na^+-coupled transport mechanism represents a broadly conserved feature of the BCCT family. Our findings provide mechanistic insights into sodium-driven substrate uptake and marine sulfur cycling.

Subject Categories Evolution & Ecology; Microbiology, Virology & Host Pathogen Interaction; Structural Biology
https://doi.org/10.1038/s44318-026-00798-w
Received 28 July 2025; Revised 11 April 2026;
Accepted 21 April 2026
Published online: 08 May 2026

Introduction

Dimethylsulfoniopropionate (DMSP) is a ubiquitous organosulfur compound in the Earth's marine environment that plays an important role in the global sulfur cycling (Curson et al, 2011; Teng et al, 2021). Over eight billion tons of DMSP are produced annually by diverse marine algae, some bacteria, corals, and plants (Galí et al, 2015; Zhang et al, 2019), constituting up to 10% of the fixed carbon in certain oceanic regions (Archer et al, 2001; Simó et al, 2002). These organisms produce and accumulate DMSP, which has diverse roles in osmoprotection, cryoprotection, oxidative stress protection, and hydrostatic pressure mitigation (Cosquer et al, 1999; Stefels, 2000; Sunda et al, 2002; Zheng et al, 2020). As a result of cell senescence, mortality, or viral lysis, DMSP is released into the environment, where it reaches nano-micromolar concentrations. In bulk seawater, DMSP concentrations are typically in the range of 10–200 nM; however, substantially higher concentrations, often reaching the micromolar range, can be found in localized microenvironments such as phytoplankton phycospheres and decaying algal particles (Gao et al, 2020; Güell-Bujons et al, 2024; Hopkins et al, 2023; Kiene et al, 2019; Zhang et al, 2019). This environmental DMSP is imported, often concentrated to millimolar concentrations (Kiene et al, 2000), and utilized for its antistress properties or as a major nutrient by marine microorganisms (Zhang et al, 2019). In the latter scenario, microbial DMSP catabolism is a major source of reduced carbon and sulfur for assimilation (Wirth et al, 2020) and climate-active gases, including methanethiol via DMSP demethylation and over 300 million tons of DMS annually via DMSP cleavage (Curson et al, 2011). Approximately 10% of produced dimethylsulfide (DMS) is released into the atmosphere (Curson et al, 2011; Kiene et al, 2000), where its oxidation products act as cloud condensation nuclei (Mungall

[1]MOE Key Laboratory of Evolution and Marine Biodiversity, State Key Laboratory of Marine Food Processing and Safety Control, College of Marine Life Sciences & Frontiers Science Center for Deep Ocean Multispheres and Earth System, Ocean University of China, Qingdao, China. [2]Marine Biotechnology Research Center, State Key Laboratory of Microbial Technology, Shandong University, Qingdao, China. [3]Laboratory for Marine Biology and Biotechnology, Qingdao Marine Science and Technology Center & Laoshan Laboratory, Qingdao, China. [4]Antarctic Great Wall Ecology National Observation and Research Station, Polar Research Institute of China, Ministry of Natural Resources, Shanghai, China. [5]State Key Laboratory of Genetics and Development of Complex Phenotypes, Collaborative Innovation Center of Genetics and Development, Department of Physiology and Neurobiology, School of Life Sciences, Fudan University, Shanghai, China. [6]School of Life Sciences, Department of Chemical Biology, Southern University of Science and Technology, Shenzhen, China. [7]School of Biological Sciences, University of East Anglia, Norwich, UK. [8]Quadram Institute Bioscience, Norwich Research Park, Norwich, UK. [9]Institute of Systems, Molecular and Integrative Biology, University of Liverpool, Liverpool, UK. [10]These authors contributed equally: Yu-Zhong Zhang, Wen-Jing Zhu, Kang Li.✉E-mail: zhangyz@sdu.edu.cn; luning.liu@liverpool.ac.uk; wangpeng3331@ouc.edu.cn

et al, 2016; Veres et al, 2020) to influence the Earth's albedo and climate (Hopkins et al, 2023; Veres et al, 2020) and are returned to land in rain and snowfall to complete the sulfur cycle. While many DMSP producers can catabolize DMSP, the majority of DMSP catabolism is thought to be driven by bacteria that import DMSP from the environment (Bullock et al, 2017; Reisch et al, 2011; Shaw et al, 2022).

Recent studies have shed light on the biodiversity and molecular mechanisms of DMSP production and catabolism in bacteria and algae (Carrión et al, 2023; Curson et al, 2011; Shaw et al, 2022). However, there are few mechanistic studies on DMSP import, which is intrinsically necessary for most of the global DMSP catabolism. Indeed, all primary DMSP cleavage and demethylation enzymes have K_m values of 0.5 to 2 mM (Yoch et al, 1997), and, thus, require intracellular concentration of DMSP to mM levels (Reisch et al, 2008; Sun et al, 2016; Yoch, 2002) that far surpass those in seawater (Belviso et al, 1993; Taylor and Gilchrist, 1991). Two distinct protein families of transporters are known to import DMSP: the betaine-carnitine-choline transporter (BCCT) family and the ATP-binding cassette (ABC) transporter system (Sun et al, 2012), the genes of which are often linked to DMSP lyase genes in bacteria that assimilate DMSP (Curson et al, 2010; Todd et al, 2010; Todd et al, 2007). Representative transporters of the BCCT family, such as *Marinomonas* sp. MWYL1, *Halomonas* sp. HTNK1 and *Vibrio parahaemolyticus* RIMD2210633 and the ABC family from *Ruegeria pomeroyi* DSS-3, *Burkholderia ambifaria*, and *Bacillus subtilis* have been shown to import DMSP in various genetic studies (Broy et al, 2015; Cosquer et al, 1999; Li et al, 2023; Todd et al, 2010; Todd et al, 2007). This study focuses on the BCCT family transporter DddT in organisms such as *Marinomonas*, *Halomonas*, *Psychrobacter*, and *Pseudoalteromonas*, which cleave DMSP to generate DMS and assimilate carbon from DMSP, whose *dddT* genes cluster with the DMSP lyase *dddD* or *dddX* and ancillary DMSP catabolic genes, there have been no gene mutagenic studies on *dddT* (Curson et al, 2010; Curson et al, 2011; Li et al, 2021; Todd et al, 2010; Todd et al, 2007). There is also an absence of detailed biochemical, structural, and dynamic simulation analysis for DddT. The physiology and molecular mechanisms of DddT-dependent DMSP transport have not been well characterized.

BCCT family transporters are common in diverse prokaryotes and eukaryotes, and often require ion gradients for function, aiding survival in environments with high osmotic pressure (Ziegler et al, 2010). The glycine betaine transporter BetP from *Corynebacterium glutamicum* is the best-characterized sodium symporter in the BCCT family (Krämer and Morbach, 2004; Ressl et al, 2009). Although extensive mechanistic studies have proposed that the transport mechanism of BetP involves two sodium ion-binding sites, Na1 and Na2, the location of Na1 has not yet been directly visualized in any structure to date (Khafizov et al, 2012; Perez et al, 2014; Perez et al, 2012). There is significant amino acid diversity within the BCCT family of transporters, and subsequent variations exist in their mechanisms and substrate range; for example, BetT is a proton-coupled transporter (Chen and Beattie, 2008), BetP is a sodium-coupled betaine transporter (Khafizov et al, 2012), and CaiT is a Na^+-independent substrate/product antiporter (Kalayil et al, 2013; Schulze et al, 2010). Given this variation in the action of the BCCT-family transporters, there is a critical need to gain a mechanistic understanding of DMSP transport by DddT.

Here, we investigated the roles of DddT in the import and catabolism of DMSP in *Psychrobacter* sp. D2, a marine gammaproteobacterium isolated from Antarctic samples, cleaves and utilizes DMSP as a carbon source (Li et al, 2021). The ability of *P.* sp. D2 DddT to import DMSP and its requirement for the sodium gradient D2 DddT protein was further characterized. Three-dimensional DddT structures were resolved using cryo-electron microscopy in different states of DMSP transport, including the closed, DMSP-bound closed, inward-open, and outward-open conformations. Analyses of these structures highlighted a transport mechanism involving two sodium ions, one coordinated by a previously uncharacterized binding site. Furthermore, bioinformatic analysis was conducted to examine the ubiquity of the conserved sodium-binding sites among diverse DddT-like proteins within organisms and environments. This work implies that DddT-like proteins and their associated processes, as identified in this study, are widespread and play a significant role in the Earth's marine environment.

Results and discussion

Function of DddT from *P.* sp. D2

The *dddT* gene is the last of the four *dddBCXT* operons (Fig. 1A) in *P.* sp. D2, whose transcription was induced by DMSP (Li et al, 2021). This operon has been suggested to allow *P.* sp. D2 to import (via DddT), cleave (via DddX) DMSP, and assimilate 3-hydroxypropionyl-CoA (via DddBC) as the carbon source (Appendix Fig. S1) (Li et al, 2021). When DMSP was provided as the sole carbon source, *P.* sp. D2 grew more slowly than in nutrient-rich 2216E medium, but faster than on other typical single-carbon sources such as succinate or glucose (Appendix Fig. S2).

DddT is a BCCT-family protein that shares 42% amino acid sequence identity with *Halomonas* sp. HTNK1 DddT, which was previously shown to import DMSP when expressed in *E. coli* (Todd et al, 2010) (Appendix Fig. S3A). The *P.* sp. D2 *dddT*-deletion mutant (Δ*dddT*), in which 1584 bp internal to this gene was deleted via homologous recombination (Appendix Fig. S4), was examined to be capable of importing DMSP, utilizing DMSP as the sole carbon source, and cleaving DMSP compared to the wild-type strain and Δ*dddT* genetically complemented with cloned *dddT* (Δ*dddT*/pBBR1MCS2-*dddT*). The Δ*dddT* mutant grew remarkably slower than the wild-type strain, and its growth could be restored to levels similar to those of the wild-type strain with the complemented strain (Δ*dddT*/pBBR1MCS2-*dddT*) (Fig. 1B). Following extended incubation, the Δ*dddT* mutant achieved comparable final optical densities as the wild-type strain. Consistently, extracellular DMSP levels were similar and depleted more rapidly (Fig. 1C) in both the wild-type and Δ*dddT*/pBBR1MCS2-*dddT* strains. These two strains also accumulated twice the amount of DMSP (Fig. 1E) compared to Δ*dddT* during these growth experiments. Furthermore, the wild-type and Δ*dddT*/pBBR1MCS2-*dddT* strains produced higher levels of DMS than the Δ*dddT* strain during the exponential growth phase (21 h) (Fig. 1D). These results indicate that the DddT protein in *P.* sp. D2 is essential for optimal growth when DMSP is the only available carbon source, as well as for the breakdown of DMSP. However, these findings also suggest the

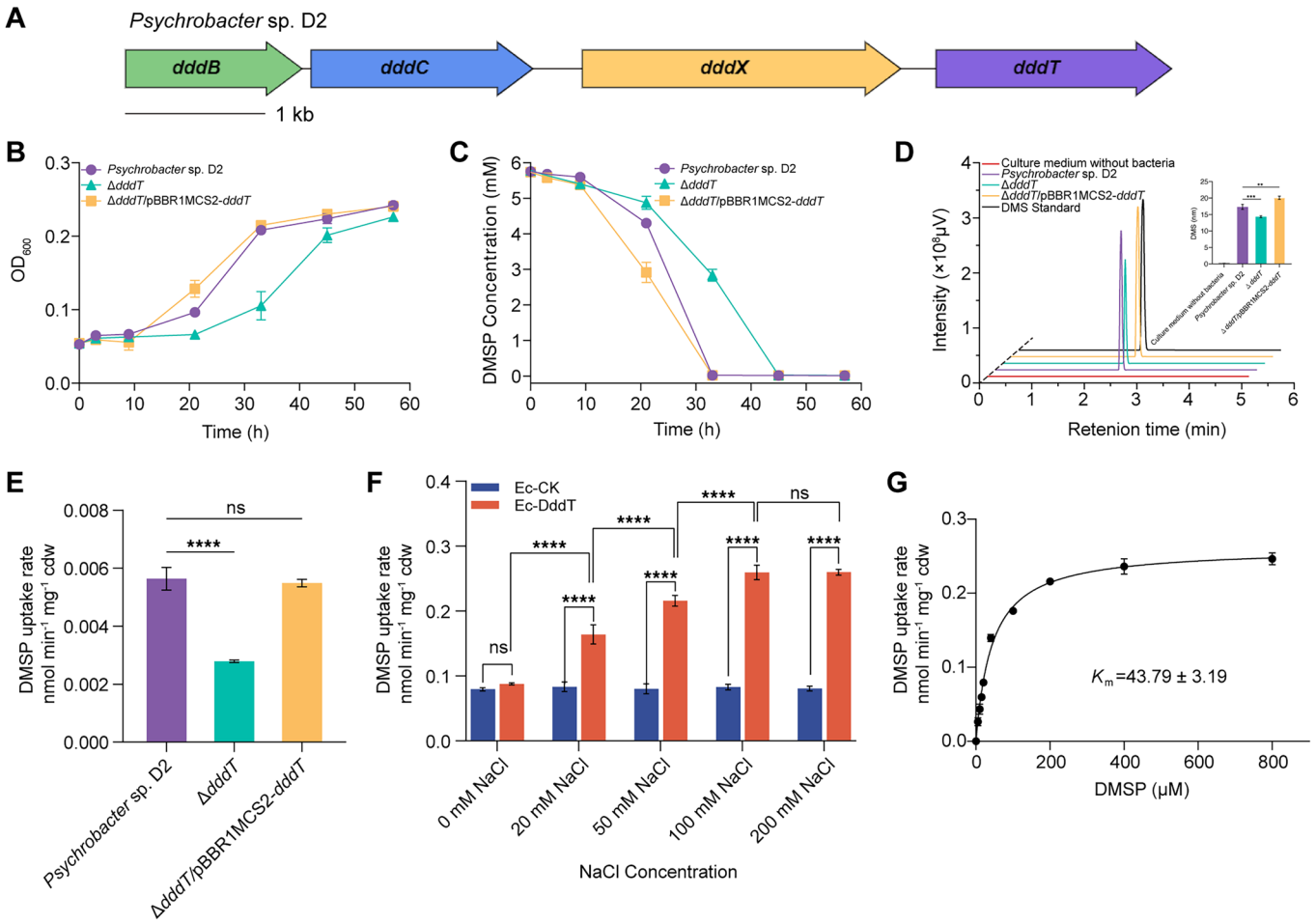

Figure 1. Role of *dddT* in *P.* sp. D2 DMSP transportation.

(**A**) DMSP catabolic operon *dddBCXT* in *P.* sp. D2. (**B**, **C**) Growth curves (**B**) and DMSP utilization (**C**) of wild-type *P.* sp. D2 strain, Δ*dddT* mutant, and the complemented mutant (Δ*dddT*/pBBR1MCS2-*dddT*). All cultures were cultivated with 6 mM DMSP as the sole carbon source. (**D**) DMS production of wild-type *P.* sp. D2 strain, Δ*dddT* mutant, and the complemented mutant after 21 h culture in the medium with 6 mM DMSP as the sole carbon source. (**E**) DMSP uptake rates of *P.* sp. D2, Δ*dddT* mutants, and the complemented mutant. cdw is short for cell dry weight. (**F**) DMSP uptake rates of *E. coli* DH5α cells with cloned *dddT* or empty vector at varying sodium levels. (**G**) DMSP uptake rates of *E. coli* DH5α cells with cloned *dddT* or empty vector under saturated sodium ion conditions (200 mM NaCl) and different DMSP concentrations. Data information: (**B–G**) Data are presented as the mean ± SD of triplicate determinations. (**D**) Statistical analysis was performed using one-way ANOVA (*P.* sp. D2 vs. Δ*dddT*, $p = 0.0001$; *P.* sp. D2 vs. Δ*dddT*/pBBR1MCS2-*dddT*, $P = 0.0015$). (**E**) Statistical analysis was performed using one-way ANOVA (*P.* sp. D2 vs. Δ*dddT*, $P < 0.0001$; *P.* sp. D2 vs. Δ*dddT*/pBBR1MCS2-*dddT*, $P = 0.6772$). (**F**) Statistical analysis was performed using two-way ANOVA (****$P < 0.0001$; 0 mM NaCl (Ec-CK) vs. 0 mM NaCl (Ec-DddT), $P = 0.9731$; 100 mM NaCl (Ec-DddT) vs. 200 mM NaCl (Ec-DddT), $P > 0.9999$). Source data are available online for this figure.

presence of alternative DMSP transport mechanisms, as other transporters may compensate for the absence of DddT, allowing the Δ*dddT* mutant to eventually utilize DMSP, albeit less efficiently.

To further study the activity of DddT, *P.* sp. D2 *dddT* was cloned into the pET-22b vector, with its promoter replaced by the constitutive promoter BBa-J23111, a moderate-strength promoter widely used for stable gene expression in *E. coli*. *E. coli* cells harboring cloned *dddT* (Ec-DddT) displayed significantly higher transport activity than those harboring the empty plasmid (Ec-CK) but only in the presence of NaCl (Fig. 1F). Moreover, DddT-mediated DMSP import was enhanced as the NaCl concentration was increased to 100 mM; beyond this concentration, the DMSP import rate remained constant, suggesting that it likely reached its maximum (Fig. 1F). These data indicate that DddT is a sodium-ion-gradient-dependent transport protein that acts as a sodium-coupled symporter, similar to most BCCT-family transporters (Ziegler et al, 2010). Under saturated sodium ion conditions, the apparent Michaelis constant (K_m) of DddT for DMSP transport was 43.79 ± 3.19 μM (Fig. 1G).

Although DddT exhibits a relatively high apparent K_m value compared with bulk seawater DMSP concentrations, localized microenvironments such as phytoplankton phycospheres and decaying algal particles can reach much higher DMSP levels, representing one of the common habitats for *Psychrobacter* species (Gao et al, 2020; Güell-Bujons et al, 2024; Heuchert et al, 2004; Hopkins et al, 2023; Katsuhiro et al, 2024; Kiene et al, 2019; Zhang et al, 2019). Moreover, in heterologous *E. coli* uptake assays, DddT displayed a V_{max} of ~0.25 nmol min^{-1} mg^{-1} cdw, substantially lower than that of BetP for glycine betaine (~83 nmol min^{-1} mg^{-1} cdw) (Perez et al, 2014). Uptake rates normalized per mg bacterial dry

weight can be remarkably influenced by differences in expression, folding efficiency, and membrane insertion in the heterologous system. Therefore, the numerical difference may not reflect a biologically relevant disparity.

Taken together, despite the relatively low observed transport rate and high apparent K_m, DddT functions as an important DMSP transporter in *P.* sp. D2, enabling efficient utilization of DMSP under relevant environmental conditions, while alternative transport mechanisms may partially compensate in its absence.

Overall structure of DddT

To study the molecular mechanism of DddT-mediated DMSP transport and its dependence on sodium ion gradients, we expressed and purified recombinant *P.* sp. D2 DddT proteins from *E. coli* C43 (DE3) for structural analysis. The DddT protein, which contains 527 amino acids and has a theoretical molecular weight of 57.7 kDa, exhibited an apparent molecular weight of approximately 39 kDa on SDS-PAGE (Appendix Fig. S3B). Furthermore, gel filtration chromatography analysis revealed that DddT exists as a trimer in solution, consistent with typical members of the BCCT family (Ressl et al, 2009; Schulze et al, 2010) (Appendix Fig. S3C).

Next, the DddT structure was resolved to 2.8 Å resolution by cryo-electron microscopy single-particle analysis (Fig. 2A; Appendix Figs. S5 and S6; Appendix Table S1), revealing that DddT adopts a closed substrate-free state (C_c) in a buffer containing 20 mM Tris-HCl (pH 8.0), 200 mM NaCl, and 0.02% n-dodecyl-β-D-maltopyranoside (DDM). For cryo-EM data processing, C3 symmetry was not imposed during the initial refinement. The map was first reconstructed in C1, and the three protomers were compared, revealing no notable conformational differences. Based on this observation, C3 symmetry was subsequently applied to improve map quality and final resolution. The DddT protein comprises three monomers, each of which adopts a cylindrical shape with 12 transmembrane (TM) α-helices (TMH1-TMH12), a bent α-helix (H1) situated on the cytoplasmic membrane surface, two short α-helices (EH1 and EH2) on the periplasmic side, and a short α-helix (IH1) on the cytoplasmic side, exhibiting C3 symmetry with an axis perpendicular to the membrane plane (Fig. 2A,C). TMH1, TMH6, and TMH11 are nearly perpendicular to the membrane, whereas TMH5, TMH7, TMH10, and TMH12 are strongly tilted (Fig. 2B). TMH3, with a local unwinding segment in the middle of the membrane, was divided into intracellular-facing (TMH3i) and extracellular-facing (TMH3e) helices (Fig. 2B). The cytoplasmic loop connecting both TMH4 and TMH5 contains a short α-helix (IH1) and a periplasmic loop that links TMH9 and TMH10, incorporating two short α-helices (EH1 and EH2) (Fig. 2B,C).

DddT exhibits a LeuT-like folding pattern (Alamo et al, 2022), resembling other BCCT-family transporters, such as BetP and CaiT (Khafizov et al, 2012; Perez et al, 2012; Ressl et al, 2009; Schulze et al, 2010; Tang et al, 2010), and other sodium symporters, such as LeuT (Krishnamurthy and Gouaux, 2012; Yamashita et al, 2005), DAT (Wang et al, 2015a), SERT (Coleman et al, 2016), MhsT (Malinauskaite et al, 2014), and GlyT1 (Shahsavar et al, 2021) from the Neurotransmitter-Sodium Symporter family, SiaT (Wahlgren et al, 2018), and vSGLT (Faham et al, 2008) from the Sodium-Solute Symporter family, and Mhp1 (Weyand et al, 2008) from the Nucleobase-Cation Symporter-1 family. This fold features five TM helices in topological repeats connected by a pseudo-dyad axis parallel to the membrane surface (Alamo et al, 2022). In DddT, TMH3-TMH7 and TMH8-TMH12 were linked by a pseudo-dyad double-symmetric axis on the membrane plane, with TMH3-TMH7 as the first segment and TMH8-TMH12 as the second segment (Fig. 2D; Appendix Fig. S7A). TMH3 and TMH4 formed a V-shaped helix pair, whereas TMH8 and TMH9 formed an inverted V-shape, tightly nested to create a four-helix bundle (Appendix Fig. S7B). The central structure of DddT is composed of this cluster, which is encircled and reinforced by TMH5-TMH7 and TMH10-TMH12.

DddT conformations in distinct transport intermediate states

To investigate the dynamic transport process of DddT, we manipulated buffer compositions, introduced substrates, and introduced amino acid substitutions, allowing capture of four additional DddT structures beyond the C_c state (Fig. 3A; Appendix Table S1). Inclusion of DMSP in NaCl buffer enabled capture of DddT in a closed, substrate-bound conformation (C_cS) (Fig. 3A; Appendix Figs. S8 and S9; Appendix Table S1). When NaCl was replaced with KCl in the buffer, even in the presence of DMSP, DddT adopted the C_c conformation without detectable DMSP binding (C_c-K^+) (Fig. 3A; Appendix Figs. S10 and S11; Appendix Table S1). Introduction of a G101D mutation in the transport channel in the presence of NaCl allowed capture of the outward-facing, substrate-free state (C_e) (Fig. 3A; Appendix Figs. S13 and S14; Appendix Table S1), whereas substitution of NaCl with KCl in the same mutant background resulted in the inward-facing state (C_i) (Fig. 3A; Appendix Figs. S15 and S16; Appendix Table S1).

In the C_cS state of DddT, a bundle of five helices formed by TMH3, TMH4, TMH5, TMH8, and TMH9 enclosed a distinct non-protein density, which was predicted to correspond to DMSP. In addition, two extra densities located between TMH3, TMH7, and TMH10 were tentatively assigned as sodium ions (Na^+) (Fig. 3E). There is a change in the transmembrane helix orientation when DMSP and Na^+ are bound, TMH3, TM6, TMH7 and TMH10 exhibited slight angular deviations relative to the C_c conformation, whereas TMH3, TMH7 and TMH10 were near the intracellular region and exhibited some degree of closure (Fig. 3B). Furthermore, a notable conformational transformation was observed in the hinge region connecting TMH3i and TMH3e, forming a pathway for DMSP translocation through TMH3 (Fig. 3C).

In the C_e state, the overall structure was characterized by an outward-facing cavity (Fig. 3A), and notable densities, also tentatively assigned as sodium ions, were observed in TMH3, TMH7, and TMH10. These densities were aligned with the positions of the two Na^+ ions observed in the closed C_cS state (Fig. 3A). A notable deviation of ~30° was observed in TMH11 and TMH12 near the periplasmic side, while TMH5 in its central region, together with TMH8 and TMH10, exhibited a slight angular shift, resulting in an outward opening of the substrate-binding cavity (Fig. 3B). Furthermore, the hinge region connecting TMH3i and TMH3e in the C_e state adopted a conformation similar to that observed in the C_cS state but distinct from that in the C_c state (Fig. 3C). This suggests that the conformational change in the hinge regions is associated with the binding of the two Na^+ ions rather than with DMSP binding.

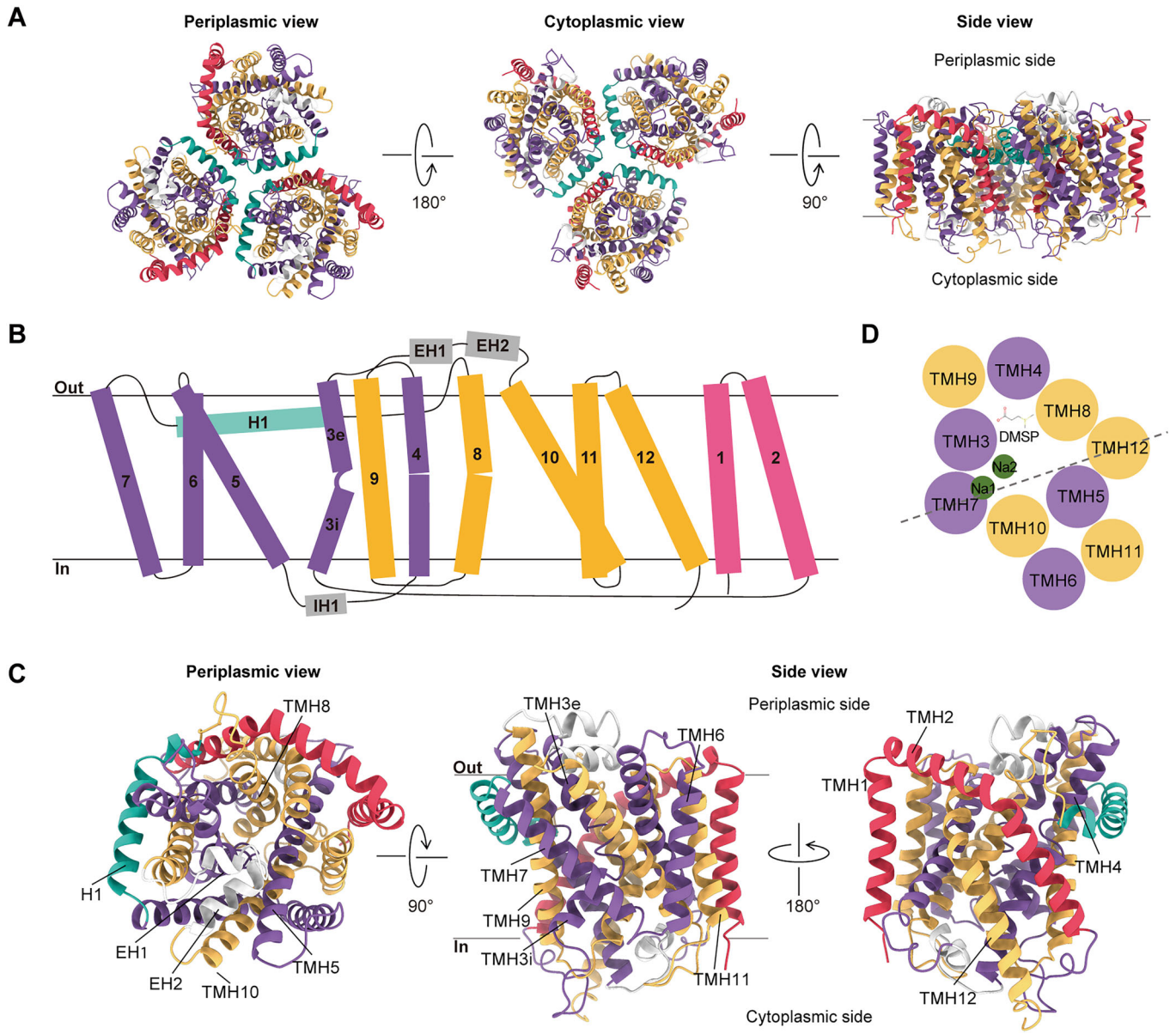

Figure 2. Overall structure of DddT.

(**A**) DddT trimer. Left, view from the periplasmic side; middle, view from the cytoplasmic side; right, side view in the membrane plane. (**B**) Schematic view of the topology of DddT. Each DddT monomer is composed of 12 transmembrane α-helices. TMH1 and TMH2 are represented in red, while TMH3-TMH7 and TM8-TMH12 are represented in purple and yellow, respectively. Cytoplasmic α-helix (IH1 and IH2) and periplasmic α-helix (EH2) are gray, and Helix 1 (H1) is blue. (**C**) DddT monomer with its distinct helices labeled. (**D**) Schematics of helix packing in LeuT-like of DddT structure, viewed from the periplasm side and at a slice through the membrane plane roughly midway across the membrane. Repeat 1 (TMH3-TMH7) and repeat 2 (TMH8-TMH12) are colored in purple and yellow, respectively. The approximate locations of ligands and sodium-binding sites are indicated by the chemical structure of DMSP and green circles, respectively.

In the C_i state, the overall structure displayed an inward-facing cavity, and due to the replacement of NaCl with KCl in the buffer, the sodium ion-binding sites corresponding to those in the C_e and C_cS states showed no detectable electron density (Fig. EV1). The distances among TMH3, TMH6, TMH7, and TMH10 increased markedly compared with those in the C_c state, contributing to the opening of the inward-facing cavity (Fig. 3B). In comparison with the Na^+-bound C_e state, this observation suggests that Na^+ binding and release regulate the structural transition of DddT between outward-open and inward-open conformations. Moreover, the hinge regions connecting TMH3i and TMH3e in the C_i state adopt an intermediate conformation between those observed in the C_c state and the C_cS/C_e states (Fig. 3C). This further supports that Na^+ binding and release play a key role in driving conformational changes in the hinge region.

In the C_c-K^+ state, although DMSP was added, no electron density corresponding to DMSP was observed, consistent with the C_c state in the presence of NaCl without DMSP (Appendix

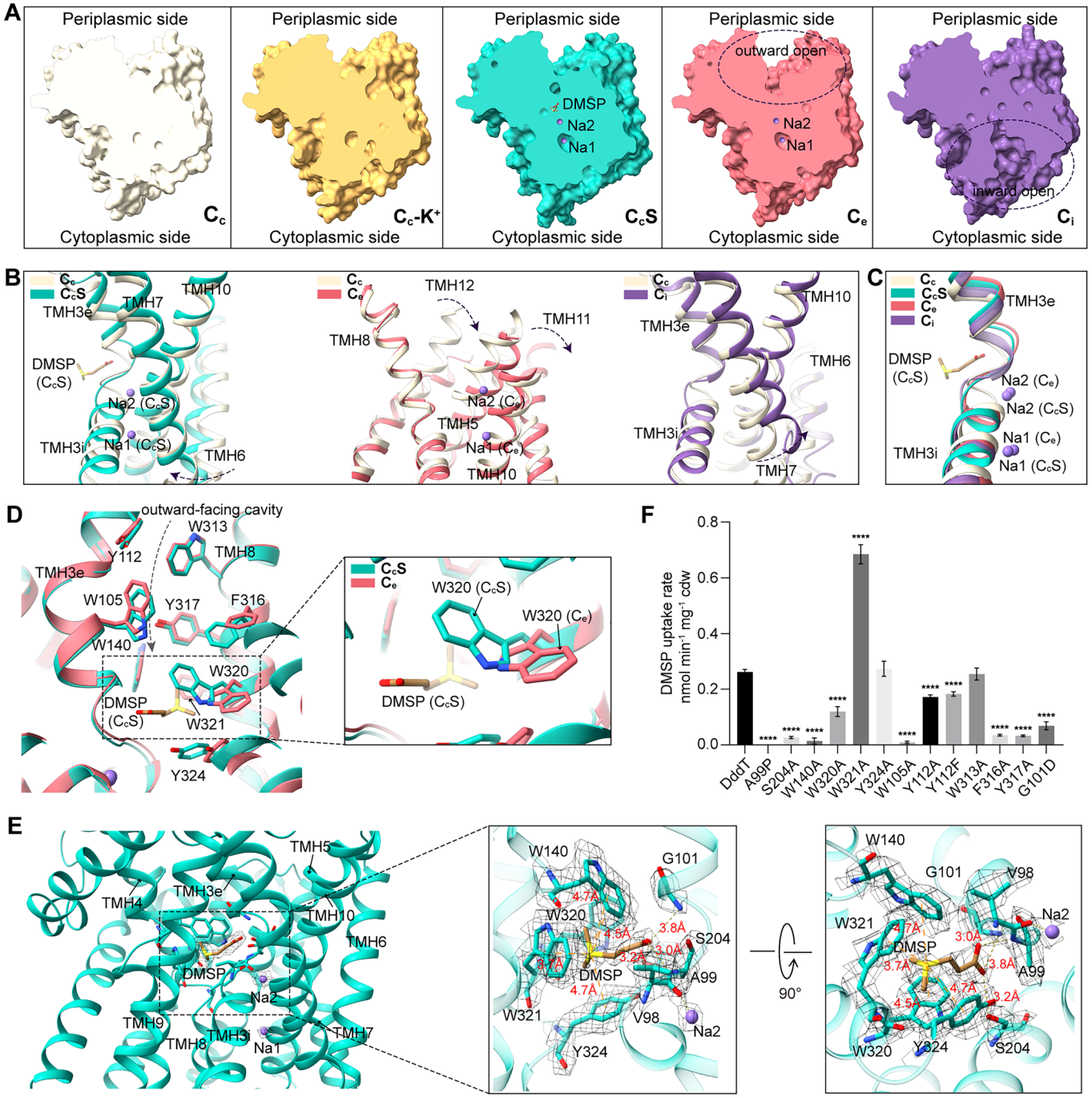

Figure 3. Conformations of DddT in different transport intermediate states and the DMSP binding site.

(**A**) Structures of DddT in different intermediate states. Cartoon views of the five DddT conformational states (C_c, C_c-K^+, C_cS, C_e, and C_i) are colored in beige, orange, blue, red, and purple, respectively. Sodium ions are shown as purple spheres. (**B**) Comparison of the conformation of TMH3, TMH6, TMH7, and TMH10 between the C_c and C_cS states, of TMH5, TMH8, TMH10, TMH11, and TMH12 between the C_c and C_e states, and of TMH3, TMH6, TMH7, and TMH10 between the C_c and C_i states. (**C**) Comparison of the hinge regions that connect TMH3i and TMH3e within the four states of DddT. (**D**) Comparison of the DMSP binding sites between the C_e state (red) and the C_cS state (blue) of DddT. The extracellular cavity is indicated by a dashed arrow. Residues involved in substrate binding on the extracellular cavity are shown as sticks. (**E**) The DMSP binding site of the C_cS state. Hydrogen bonds are represented by yellow dashed lines. The distances between DMSP and the aromatic box residues are shown as orange dashed lines. The gray mesh shows the local cryo-EM density around DMSP, Na^+ (Na2), and the residues involved in sodium binding, contoured at 7 root-mean-square-deviation (RMSD). (**F**) The DMSP uptake rates of DddT and site-directed mutants in predicted DMSP binding residues. The transport capabilities of these mutants were assessed and normalized against expression levels of DddT and its mutants based on western blot analysis. Data are presented as the mean ± SD of triplicate determinations. Statistical analysis was performed using one-way ANOVA (****$P < 0.0001$; DddT vs. Y324A, $P = 0.9699$; DddT vs W313A, $P = 0.9997$). Source data are available online for this figure.

Fig. S12). Owing to the limitations of single-particle cryo-EM, we cannot completely exclude a minor population of DMSP-bound particles in the KCl sample. However, particle classification and reconstruction indicate that a huge number of particles adopt a DMSP-free conformation. In addition, only this population could be aligned and refined to high resolution, suggesting that the remaining particles likely represent conformationally unstable states. This contrasts sharply with the NaCl condition with DMSP, under which only the DMSP-bound conformation could be aligned and refined to high resolution. Taken together with data of the C_c, C_cS, C_i, and C_e states, these findings suggest that stable DMSP binding requires Na^+, whereas stable Na^+ binding in turn depends on either DMSP or mutations in TMH3 (e.g., G101) that perturb the hinge region (Figs. 3A and EV2). Thus, DMSP binding, Na^+ binding, and hinge conformation change are tightly coupled.

DMSP binding sites in DddT

As mentioned above, DMSP densities were identified in the structures of the closed C_cS state of DddT. DMSP is proposed to enter the binding site via the outward-facing cavity of the C_e state. Structural analysis of this cavity revealed that aromatic amino acid residues, including Trp105 and Tyr112 on TMH3, as well as Trp313, Phe316, and Tyr317 on TMH8, are likely key residues involved in the DMSP entry pathway (Fig. 3D). These residues are presumed to direct DMSP towards a potential aromatic binding pocket formed by Trp320, Trp321, Trp140, and Tyr324 (Fig. 3D,E). In the C_cS state, DMSP is bound within this pocket, where Arg320, Trp321, Trp140, and Tyr324 form cation–π interactions with the sulfonium (S^+) group of DMSP, while the side chain of Ser204 and the backbone amide nitrogens of Gly101 and Ala99 form hydrogen bonds with the carboxyl group of DMSP (Fig. 3E). To investigate in depth the roles of these amino acids in DMSP binding, substitution mutations were made in these residues and the transport capabilities of these mutants were assessed, normalized against expression levels of DddT and its mutants based on western blot analysis (Appendix Fig. S17). The results indicated a reduction in transport activity for most mutants compared to wild-type DddT. The A99P, S204A, W140A, W320A, Y112A, Y112F, W105A, F316A, Y317A, and G101D mutants exhibited a significant loss of activity, confirming the critical role of these amino acid residues in DMSP transport (Fig. 3F). Notably, the W321A mutant exhibited enhanced transport activity, suggesting that Trp321 may not play a critical role in DMSP binding and transport. The mechanistic basis for this phenotype merits further investigation.

Compared to the C_e state, the C_cS state exhibits a pronounced conformational change at Trp320 within the DMSP-binding pocket (Fig. 3D), indicating that Trp320 not only constitutes a critical part of the functional binding site for DMSP but also may contribute to promoting its movement during the transport process.

Na^+-binding sites in DddT

As described above, electron density consistent with putative Na^+ ions was observed in the C_cS and C_e states. Removal of Na^+ from the buffer abolished this density in the C_c–K^+ and C_i states at the corresponding position, further strengthening its assignment as Na^+. While the putative Na2 site in DddT is similar to that found in BetP (Fig. 4A), DddT lacks the BetP Na1 site, and the key residues T246 and T250 necessary for sodium binding are absent (Khafizov et al, 2012; Perez et al, 2014; Perez et al, 2012). Residues Ile197 and Ala201 of DddT, which correspond to the Na1 site of BetP, are hydrophobic and are unable to bind sodium ions (Fig. 4A). In addition, there were no other suitable locations for sodium binding near the BetP Na1 equivalent region in DddT. Instead, we found that DddT has a putative Na1 site closer to the cytoplasmic side. Structural analysis of the C_cS and C_e states suggests that Na1 binding is coordinated by the backbone carbonyl oxygen of Met92 (TMH3); the backbone carbonyl oxygen of Leu252, via a water molecule, and the side chain of Ser256 (TMH7); and the backbone carbonyl oxygen of Thr418, the side chain of Asp421 through a water-mediated interaction, and the side chain of Ser422 (TMH10). Whereas Na2 coordination is presumed to involve the backbone carbonyl oxygens of Cys95 and Val98 (TMH3) and Phe415, together with the side chains of Thr418 and Thr419 (TMH10) (Fig. 4B). Based on the observed coordination environment, Na2 coordination appears relatively stable, whereas Na1 shows longer coordination distances and correspondingly less stable binding. Such variability in Na^+ coordination is not unusual and has been observed in other transporters. For example, in the BetP transporter, the proposed Na1 site displays a coordination pattern distinct from that of the stable Na2 site (Perez et al, 2014). This instability may be functionally relevant, as discussed in detail below in another section.

To further confirm the Na1 and Na2-binding sites and their functional significance during the transport process, substitution mutants of the residues involved in coordination were generated, and their impact on DddT DMSP transport capability was investigated. Alanine is our primary choice for mutagenesis of these residues. However, for amino acids whose backbone amide oxygen atoms participate in metal ion coordination, alanine substitutions may not significantly disrupt the ion-binding environment. Therefore, we selectively introduced proline mutations, as proline's rigid backbone is more likely to interfere with backbone-mediated interactions, providing additional biochemical insight. It should be noted, however, that proline substitutions are relatively drastic and have intrinsic limitations. Such substitutions may cause structural effects beyond modification of the peptide bond amide group; therefore, the validation results should be regarded as reference evidence only.

For the mutants involved in Na1-binding and Na2-binding, the transport capabilities were normalized to DddT expression levels (Appendix Fig. S17). For the Na1-binding site, assays conducted under various sodium gradients revealed that the M92P, L252P, S256A, T418P, D421A, and S422A mutations, which are associated with Na1 binding, led to marked changes in DddT transport activity (Fig. 4C,D; Appendix Table S2). For the Na2-binding site, mutations of residues involved in coordinating this site, including C95P, A99P, and F415P, completely abolished DddT transport activity (Fig. 4D). Other mutations at the Na2 site, specifically V98P and T419A, retained residual transport activity but led to a notable reduction in transport activity under varying sodium gradient conditions (Fig. 4C,D; Appendix Table S2). Interestingly, the T418A mutant exhibited a higher V_{max} relative to wild-type DddT under conditions of a high sodium gradient, whereas it showed reduced transport activity under low sodium gradient conditions (Fig. 4D; Appendix Table S2). This variation suggests that the T418A mutation increases the dependence on a high

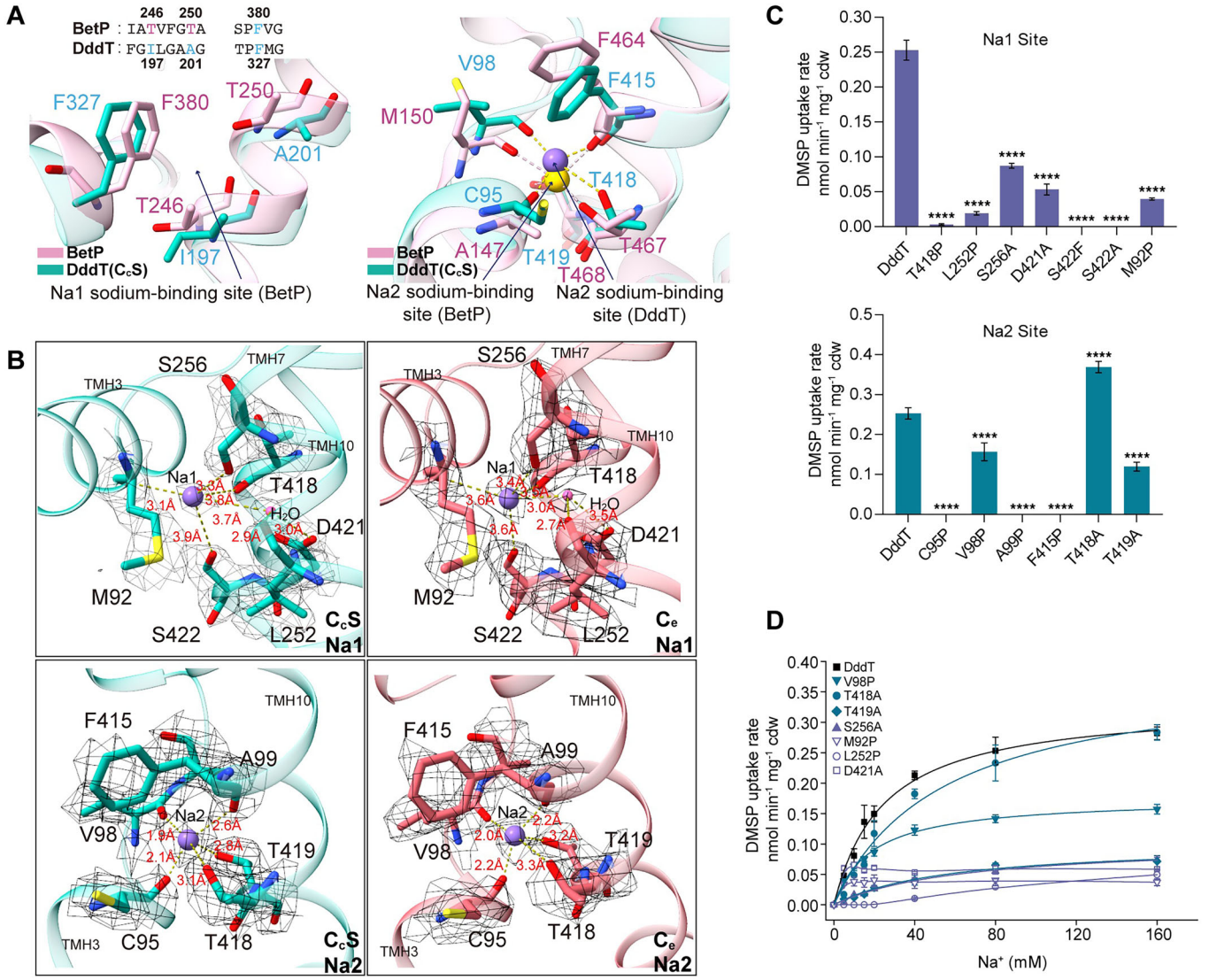

Figure 4. The sodium-binding sites in DddT.

(A) Structure comparison of BetP and DddT around the BetP Na1 and Na2 sodium-binding sites. The residues of the C_cS state of DddT and BetP (PDB ID: 4AIN) are colored blue and pink, respectively. The sodium ions in Na2 sodium-binding sites of DddT (C_cS) and BetP are shown as purple and yellow spheres, respectively. **(B)** Comparison of the Na^+-binding sites in the C_cS (blue) and C_e (red) states of DddT. Sodium ions and H_2O molecules are shown as purple and pink spheres, respectively. Residues involved in sodium binding are shown as sticks. The gray mesh shows the local cryo-EM density of Na^+ (Na1, Na2), H_2O molecules, and the residues involved in sodium binding, contoured at 8 RMSD. **(C)** DMSP uptake rates of DddT and various site-directed mutant derivatives under saturated sodium ion and DMSP conditions. The transport capabilities of these mutants were assessed and normalized against expression levels of DddT and its mutants based on western blot analysis. Data are presented as the mean ± SD of triplicate determinations. Statistical analysis was performed using one-way ANOVA (****$P < 0.0001$). **(D)** DMSP uptake rates of DddT and various site-directed mutant derivatives under saturated DMSP and different sodium ion concentrations. The transport capabilities of these mutants were assessed and normalized against expression levels of DddT and its mutants based on western blot analysis. Data are presented as the mean ± SD of triplicate determinations. The kinetic parameters of sodium ion binding of DddT mutants are summarized in Appendix Table S2. Source data are available online for this figure.

sodium gradient while compromising transport efficiency when sodium availability is limited. Collectively, these findings highlight the critical roles of the Na1 and Na2-binding sites in enabling efficient DMSP transport.

The role of the two Na^+ ions

Na1 was observed in the C_cS and C_e states, but not in the C_c, C_c-K^+, or C_i states (Fig. 3A). Structurally, the Na1 site, strategically located between TMH3, TMH7, and TMH10, appears to help stabilize these three helices, which can move apart to form the inward-facing cavity in the C_i state. Since the key residues involved in Na2 binding are also located on these three helices, binding at Na1 and Na2 may affect each other. As described above, Na1 exhibits less stable binding. The fact that Na1 can still be identified in our cryo-EM structures is probably due to the high Na^+ concentration present on both the periplasmic and cytoplasmic sides in our sample preparation, which promotes Na1 occupancy. During the actual transport cycle, however, the

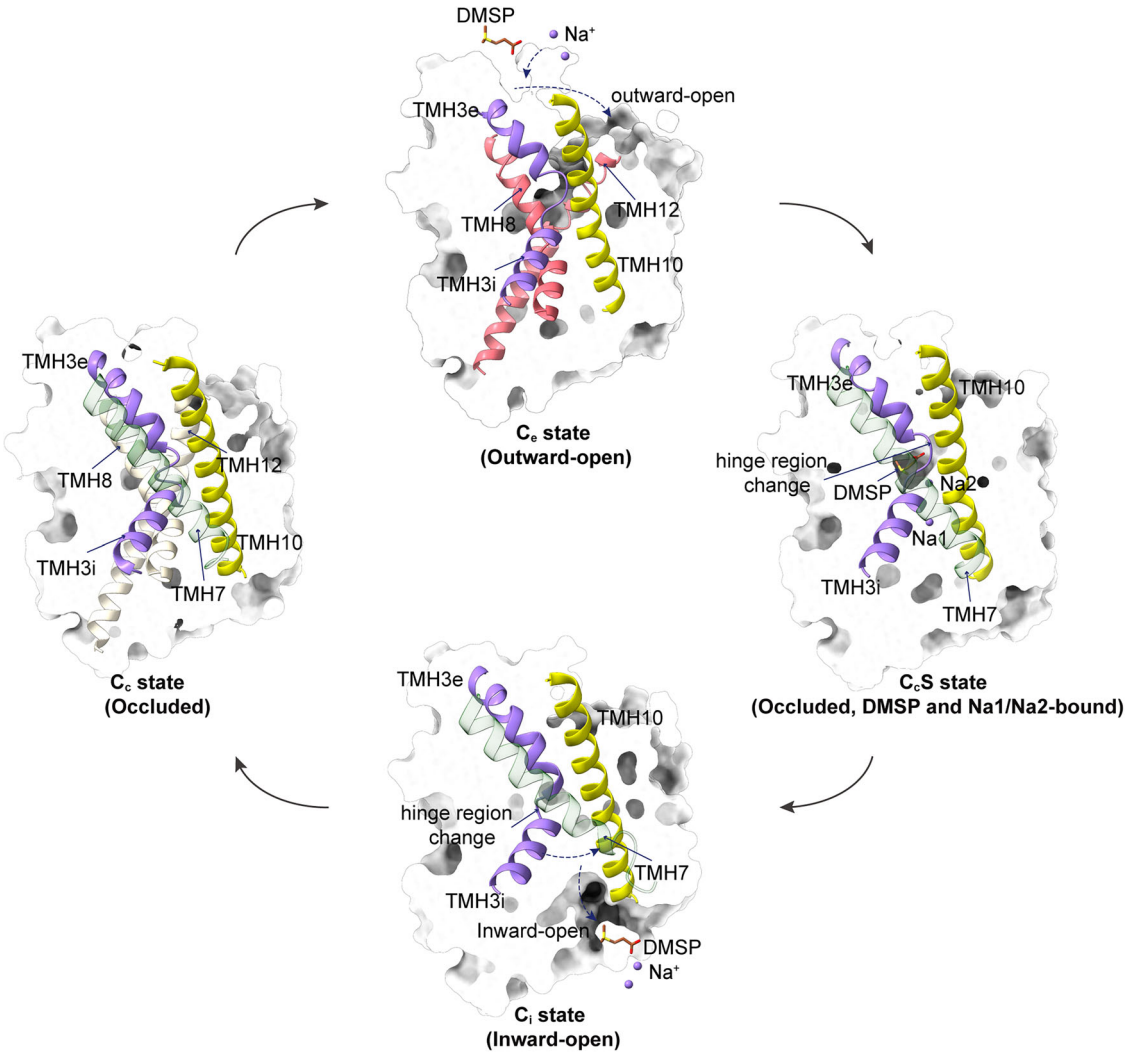

Figure 5. Proposed cartoon diagram of the transport mechanism of DddT.

TMH3 and TMH10 in the C_c, C_e, C_cS, and C_i states are highlighted in purple and yellow, respectively. TMH7 in the C_c, C_cS, and C_i states is shown in green. TMH8 and TMH12 in the C_c state are colored beige, and TMH8 and TMH12 in the C_e state are shown in red. Sodium ions are shown as purple spheres. All DddT conformational states were determined by cryo-EM in this study.

cytoplasmic Na^+ concentration is much lower, likely leading to Na1 dissociation and consequently affecting Na2 binding. For Na2, as analyzed above, the binding of DMSP and Na^+ as well as the conformational changes of the hinge region are coupled, and alteration of one component inevitably influences the other two. From the structural details, Na2 and DMSP bind to opposite sides of the TMH3 hinge region. Na2 appears to be directly involved in this coupling. The peptide bond between Val98 and Ala99 in the TMH3 hinge participates in the binding of both DMSP and Na2. The carbonyl oxygen of this peptide bond coordinates Na2, while the amide nitrogen is likely involved in DMSP binding (Fig. 3E). In the C_c state, significant conformational rearrangements in the TMH3 hinge region led to a flip of this peptide bond so that the carbonyl oxygen no longer faces the Na2 site and the amide nitrogen no longer faces the DMSP site (Fig. 3C,E). Based on these observations, we propose a cooperative function of Na1 and Na2. The relatively weak coordination of Na1 is crucial for DddT to exploit the Na^+ gradient. Moreover, because both ions are coordinated by TMH3, TMH7, and TMH10, their interplay enables Na2 to effectively harness this energy. In turn, Na2 directly contributes to the coupled process of DMSP binding and hinge conformational changes, thereby enabling substrate transport.

To further validate that both Na1 and Na2 are essential for DddT-catalyzed DMSP transport, we performed solid-supported membrane (SSM) electrophysiology assays. The results revealed that DddT mediates DMSP uptake with a stoichiometry of approximately two Na^+ ions per DMSP molecule (Appendix Fig. S18), which supports our analyses identifying two distinct Na^+-binding sites.

The DMSP transport mechanism

Based on structural analysis and biochemical validation, we proposed the DMSP transport process and mechanism of DddT (Fig. 5). When DMSP is present in an environment with an appropriate sodium gradient, DddT transitions to the C_e state,

allowing for the simultaneous entry of DMSP and sodium ions. The entry of DMSP and sodium ions is facilitated by the widening of the angle between TMH8 and TMH10. Subsequently, sodium ions rapidly bind to the Na1 and Na2 sites, the DMSP molecule binds to the TMH3 hinge region, and the TMH3 hinge undergoes a conformational change, leading DddT to transition into the C_cS state. Due to the Na^+ gradient across the membrane and the relatively low intracellular Na^+ concentration, the sodium ion at the Na1 site dissociates, resulting in instability of the TMH3, TMH7, and TMH10 helices and further destabilizing Na2 binding. Because Na2, DMSP, and the TMH3 hinge region are coupled, dissociation of Na2 triggers the release of DMSP and conformational changes in the TMH3 hinge. During this process, DMSP passes through the TMH3 hinge region, and the release of Na^+ ultimately drives the transition of DddT into the C_i state. Concurrently, a cytoplasm-facing cavity gradually forms to allow DMSP entry into the cytoplasm. Once DMSP and sodium ions have entered the cytoplasm, in the absence of mutations that stabilize the inward-facing conformations, wild-type DddT reverts to a state ready for the next transport cycle. While DddT, with its newly identified Na1 site, mediates a transport process that differs from BetP, the Na2 site plays a conserved and central functional role in both systems.

A broad implication of the transport mechanism akin to DddT

As one of the primary transporters of DMSP, DddT is distributed in numerous DMSP-metabolizing bacterial strains (Sun et al, 2012). Therefore, we first analyzed whether DddT from different bacterial strains employs the same transport mechanism. The BCCT-family transporters exhibit a high sequence similarity, and it is difficult to distinguish between different transporters for various substrates based solely on sequence similarity analysis. Therefore, we conducted gene cluster analysis. Using the representative bacterial genomes obtained from GenBank, 61 *dddT* genes were clustered with the DMSP lyase genes *dddD/dddX*. The corresponding DddT proteins were mainly distributed among gamma-proteobacteria, with Oceanospirillales and Pseudomonadales comprising a large proportion, followed by Alphaproteobacteria, with most belonging to the Rhodobacterales (Fig. 6A). This distribution pattern suggests a prominent role of DddT in various bacterial groups, particularly those associated with marine and aquatic environments.

Systematic phylogenetic analysis revealed that these DddT proteins are grouped into distinct phylogenetic branches within the BCCT family. Some of the DddT proteins were closer to the branch where BetP was located, whereas those grouped with DddT from *P.* sp. D2 were closer to the Na^+-independent substrate/product antiporter CaiT (Fig. 6B). This suggests that although these DddT proteins likely transport DMSP, there may be variations in their transport process. This was supported by a comparative analysis of the Na^+-binding sites of these DddT proteins. We found that, in addition to the typical Na2-binding site, there were differences in the Na1-binding site depending on the clustering. The corresponding residues at the BetP Na1-binding site of the DddT proteins clustered with DddT from *P.* sp. D2 were all hydrophobic residues and unable to bind Na, whereas the residues at the DddT Na1 site were relatively conserved (Fig. EV3). This indicated that they probably adopted similar Na^+-binding sites as DddT from *P.* sp. D2. In contrast, the corresponding residues at the BetP Na1-binding site of DddT proteins closer to the branch where BetP was located had at least one hydrophilic residue. This suggests that they may contain a similar Na1-binding site and possess a transport mechanism similar to that of BetP.

Subsequently, we examined DddT-like BCCT-family transporters predicted from metagenomic data obtained from sediment, polar ocean, and Tara Ocean samples. Using the sequence length as a criterion, we identified 645 sequences. Among these, 411 sequences shared similarities with DddT from *P.* sp. D2, which displayed hydrophobic residues at positions corresponding to the BetP Na1-binding site (Figs. 6C and EV4). DddT homologues are widely dispersed among the metagenomic samples in the oceans (Fig. 6D). To assess their functionality, two of these homologues were selected for DMSP transport activity analysis. However, none of them demonstrated DMSP transport activity (Appendix Fig. S19), indicating the presence of numerous BCCT-family transporters that do not transport DMSP but may employ a transport mechanism akin to DddT from *P.* sp. D2. These findings suggest that, in BCCT-family transporters, different substrates can induce variations in the transport process, while similar mechanisms can accommodate the transport of diverse substrates. These observations highlight the complexity and versatility of transport processes within the BCCT family, suggesting that the relationship between substrate specificity and transport mechanism is more nuanced than previously thought.

In summary, this study elucidates the structural basis for bacterial absorption of the important sulfur-containing organic compound DMSP via DddT. These findings deepen our understanding of DMSP transport and offer new insights into the mechanisms of the BCCT-family transporters, emphasizing the specific role of sodium.

Methods

Reagents and tools table

Reagent/resource	Reference or source	Identifier or catalog number
Experimental models		
Psychrobacter sp. D2	Zhang Laboratory	NCBI: JACDXZ000000000
Δ*dddT*	This study	
Δ*dddT*/pBBRMCS2-*dddT*	This study	
E. coli WM3064	Dehio and Meyer, 1997	
E. coli DH5α	Vazyme Biotech Company, China	Cat # C502-02
E. coli C43 (DE3)	WEIDI Biotechnology Company, China	Cat # EC1040
Recombinant DNA		
pK18*mobsacB*-Ery	Wang et al, 2015b	
pK18*mobsacB*-Ery- *dddT*	This study	
pET-22b-*dddT*	This study	
pET-22b-Bba-*dddT*	This study	
pBBR1MCS2	Kovach et al, 1995	
pBBR1MCS2-*dddT*	This study	

Reagent/resource	Reference or source	Identifier or catalog number
Antibodies		
Anti-His Tag Monoclonal antibody	Solarbio, China	Cat # K200060M
Anti-GAPDH rabbit polyclonal antibody	Sangon Biotech, China	Cat # D110016
HRP-labeled Goat Anti-mouse IgG(H + L)	Beyotime, China	Cat # A0350
HRP-labeled Goat Anti-Rabbit IgG(H + L)	Beyotime, China	Cat # A0352
Oligonucleotides and other sequence-based reagents		
PCR primers	This study	Appendix Table S3
Chemicals, enzymes, and other reagents		
FastPfu DNA Polymerase	TransGenBiotech, China	Cat # AP221-01
In-Fusion Snap Assembly Maser Mix	TaKaRa, Japan	Cat # 638947
Pierce BCA Protein Assay Kit	Thermo Fisher, USA	Cat # 23227
Software		
cryoSPARC	Punjani et al, 2017	
UCSF Chimera	Pettersen et al, 2004	
COOT	Casañal et al, 2020	
Phenix	Liebschner et al, 2019	
MolProbity 4	Williams et al, 2018	
ChimeraX	Pettersen et al, 2021	
Other		

Bacterial strains and growth conditions

P. sp. D2 and its mutants and supplemental strains were cultured in marine broth 2216E medium or the basal medium (Appendix Table S4) supplemented with 6 mM DMSP, glucose, or succinate as the carbon source at 20 °C. *E. coli* strains DH5α and C43 (DE3) were cultured in lysogeny broth (LB) medium, whereas *E. coli* strain WM3064 (Dehio and Meyer, 1997) was supplemented with 0.3 mM diaminopimelic acid. All the *E. coli* strains were cultured at 37 °C.

Gene knockout

The *dddT* gene of *P.* sp. D2 was knocked out using the suicide plasmid, pK18*mobsacB*-Ery (Wang et al, 2015b), through homologous recombination. The upstream and downstream homology arm sequences of *dddT* were PCR-amplified from *P.* sp. D2 genomic DNA using two pairs of primers, *dddT*-Up and *dddT*-Down, and the *dddT*-Up-Down homology arm fragment was obtained using the In-Fusion HD Plus Cloning Kit (Takara, USA) via gene splicing by overlap extension PCR (SOE PCR). The *dddT*-Up-Down homology arm fragment was seamlessly connected with linearized pK18*mobsacB*-Ery to construct a marker-free knockout plasmid of the *dddT* gene, which was named pK18*mobsacB*-Ery-*dddT*. The plasmid pK18*mobsacB*-Ery-*dddT* was transformed into *E. coli* WM3064 as the donor strain, whereas *P.* sp. D2 was used as the recipient strain for intergeneric conjugation.

For screening and validation of the first homologous recombination mutant, surviving colonies were selected on marine 2216E agar plates containing 25 μg/mL erythromycin and validated by PCR amplification with primers *dddT*-SF/*dddT*-SR to obtain colonies for which the pK18*mobsacB*-Ery-*dddT* plasmid was inserted into the genome of *P.* sp. D2. The mutant bacteria that underwent the first homologous recombination were cultured in Marine Broth 2216E medium and plated on Marine 2216E agar plates containing 10% (w/v) sucrose. The colonies grown on the plate were selected and screened using PCR verification with *dddT*-LF/*dddT*-LR primers to identify the monoclonal strains that had undergone the second homologous recombination. The final *dddT* mutant underwent a second homologous recombination and was sensitive to erythromycin.

Using the genomic DNA of *P.* sp. D2 as a template, *dddT* and its promoter were amplified using *dddT*-pBBR-F/*dddT*-pBBR-R primers. The PCR fragment was seamlessly ligated to linearized pBBR1MCS2 (Kovach et al, 1995) using the In-Fusion HD Plus Cloning Kit. After transformation into *Escherichia coli* DH5α, a single clone was selected and validated by sequencing to produce the pBBR1MCS2-*dddT* plasmid. The pBBR1MCS2-*dddT* plasmid was transformed into *E. coli* WM3064 and mobilized into the Δ*dddT* mutant by intergeneric conjugation. The screening plate was marine 2216E agar plates containing 80 μg/mL kanamycin, and PCR was used to verify the correctness of the complemented mutant. The same method was used to mobilize the empty vector pBBR1MCS2 into Δ*dddT*. Primers used in this study are listed in Appendix Table S3.

DMSP utilization assay

Cells were grown in Marine Broth 2216E medium, harvested by centrifugation, and washed three times with sterile artificial seawater. The washed cells were diluted to the same density of $OD_{600} \approx 2.0$, and 1% (v/v) cells were inoculated into the basal medium with 6 mM DMSP. The seeded cells were cultured at 20 °C in the dark, and samples were collected at various times. The growth of the bacteria was determined by measuring the OD_{600} using a spectrophotometer V-550 (Jasco Corporation, Japan), and the utilization of DMSP was determined by liquid chromatography after filtering with a 0.22-μm filter. For the DMS production assay, the seeded cells were cultured at 20 °C in a sealed headspace vial for 21 h, and the DMS production was detected using a gas chromatograph (GC-2030, Shimadzu, Japan) equipped with a flame photometric detector(Liu et al, 2018).

Plasmid construction for activity assay

The genomic DNA of *P.* sp. D2 was used as a template to amplify *dddT* using 22b-Bba-*dddT*-F/22b-Bba-*dddT*-R primers. The constitutive promoter BBa-J23111 was cloned upstream of *dddT*, resulting in a fragment containing *dddT* with the BBa-J23111 promoter of *E. coli*. This fragment was then inserted into the NdeI/XhoI restriction sites of pET-22b to generate the *dddT* constitutive expression plasmid pET-22b-Bba-*dddT*. The plasmids pET-22b-Bba and pET-22b-Bba-*dddT* were transferred into *E. coli* DH5α, resulting in the strains Ec-CK and Ec-DddT.

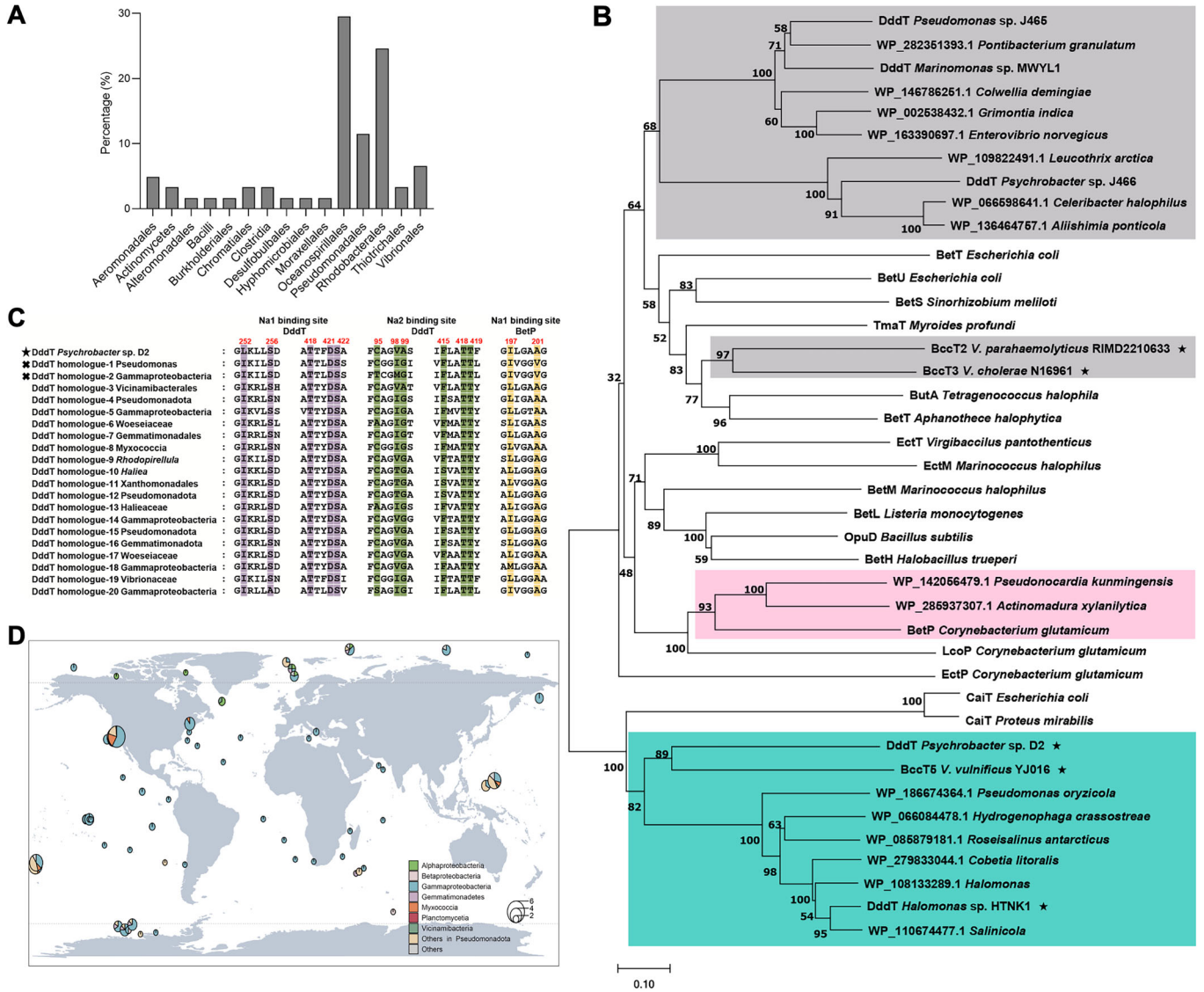

Figure 6. The broad significance of the DddT transport mechanism.

(A) The distribution of identified DddT homologues whose genes clustered with the DMSP lyase genes *dddD/dddX* in bacteria. **(B)** Phylogenetic analysis towards experimentally confirmed functional DddTs (Gregory et al, 2021; Todd et al, 2010), identified DddT homologues clustered with the DMSP cleavage enzymes DddD/DddX(Curson et al, 2010), and other BCCT family transporters (Ziegler et al, 2010). DddT homologues grouped with BetP are highlighted with gray and pink backgrounds. The DddT homologues with two hydrophilic residues at the BetP Na1-binding site are shown in pink, while those with one hydrophilic residue are shown in gray. DddT homologues grouped with *P.* sp. *D2* DddT, which have no hydrophilic residues at the BetP Na1-binding site, are highlighted with a green background. The experimentally confirmed functional DddTs are marked with ★. **(C)** Multi-sequence alignment of *P.* sp. D2 DddT and 20 randomly selected DddT homologues identified from metagenomic analysis. Key residues around the sodium-binding site are marked out. The experimentally confirmed functional DddTs are marked with ★, while the DddT homologues not involved in DMSP transport are marked with ×. The 20 sequences were randomly sampled from each major clade after taxonomic classification to ensure balanced representation. **(D)** The geographic and species distribution of the 411 DddT homologues from metagenome data. Source data are available online for this figure.

Transport assays

The *P.* sp. D2 and Δ*dddT* strains were grown at 20 °C in the marine broth 2216E medium to an OD_{600} of 0.8, whereas the complemented strain (Δ*dddT*/pBBR1MCS2-*dddT*) was cultivated in the same medium supplemented with 50 μg/mL kanamycin. Cells were diluted to the same density for uptake measurements. After adding 5 mM DMSP for 2 h at 20 °C in the dark, the cells were harvested by centrifugation, washed three times with sterile artificial seawater, and resuspended in the same volume to determine intracellular uptake of DMSP.

Ec-DddT and its mutants were cultivated at 37 °C in Luria-Bertani (LB) medium (50 μg/mL ampicillin) to an OD_{600} of 1.0. Cultured cells were harvested by centrifugation at 8000 rpm for 2 min. The cell pellets were washed three times with 25 mM KPi buffer (pH 7.5), each time resuspending the cells thoroughly and centrifuging to remove the supernatant. After the final wash, the cells were resuspended in the same KPi buffer supplemented with

20 mM glucose. The cell suspensions of both wild-type Ec-DddT and its mutants were adjusted to the same final volume and normalized to an OD_{600} of 1.0.

There were some differences in the measurement of transport activity between saturated and gradient NaCl conditions. To determine DMSP transport activity under saturated NaCl and DMSP conditions, NaCl was added to the cell suspension to a final concentration of 200 mM. For assays under gradient NaCl concentrations with saturated DMSP, varying NaCl concentrations were supplemented. Based on the NaCl concentration added, an appropriate amount of KCl was supplemented to maintain the system osmolarity at 800 mOsm/kg. Subsequent steps for the measurement of transport activity were identical. The mixtures were gently mixed and incubated at 37 °C for 3 min. DMSP was then added to a final concentration of 250 mM, followed by incubation at 37 °C. DMSP uptake was terminated 10 min after addition by collecting cells via centrifugation. Cells were washed three times with 200 mM KPi buffer to remove extracellular DMSP and finally resuspended in an equal volume of 200 mM KPi buffer for activity determination.

All samples were then assayed on a gas chromatograph (GC-2030, Shimadzu, Japan) equipped with a flame photometric detector for DMS production (Liu et al, 2018), from which DMSP uptake was calculated according to the standard curve.

Western blot detection of protein levels

Protein levels in cell extracts were analyzed using western blot. The DddT and its mutants, with C-terminal His-tag expressed on the constitutive expression plasmid pET-22b-Bba, were detected by anti-His antibodies. Ec-DddT and its mutants were cultivated at 37 °C in LB medium (50 μg/mL ampicillin) to an OD_{600} of 1.0. The cells were harvested and washed three times in 25 mM KPi buffer (pH 7.5), resuspended, and diluted in the same buffer to achieve an OD_{600} of approximately 1.0. The cells were then disrupted by a high-pressure crusher. The cell lysate was centrifuged at 20,000×*g* for 10 min, and the total protein content in the supernatant was quantified using the BCA assay. The proteins (10 μg) were separated through SDS-PAGE. Subsequently, the separated proteins were electrotransferred onto a PVDF membrane (Invitrogen, Carlsbad, CA). The membrane was blocked with QuickBlock solution (Beyotime, China) at 25 °C for 30 min and incubated with a mouse-derived anti-His monoclonal IgG1 antibody (Solarbio, China) at a 1:1000 dilution, maintained under gentle rocking at 25 °C for 2-4 h. The membrane was washed three times in TBST (Tris-Buffered Saline with Tween-20) before being incubated with HRP-conjugated goat anti-mouse IgG (Beyotime, China) secondary antibody at a 1:2000 dilution in TBST at 25 °C for 1 h. After three additional TBST washes, protein signals were visualized using BeyoECL Plus (Beyotime, China). Glyceraldehyde 3-phosphate dehydrogenase (GAPDH) was detected with an anti-GAPDH monoclonal antibody IgG1 (Solarbio, China) as the control. The expression levels of DddT and its mutants in the cells were normalized by Western blot using Image-Pro Plus software.

Gene cloning, point mutation, protein expression, and purification

The *dddT* gene was amplified using PCR from the genomic DNA of *P.* sp D2 and inserted into the NdeI/XhoI restriction sites of the pET-22b vector containing a C-terminal His tag. The G101D point mutation in DddT was introduced using polymerase chain reaction-based methods. The constructed vector was transformed into *E. coli* C43 (DE3) cells for protein expression. Cells were grown at 37 °C in LB medium supplemented with 100 μg/mL ampicillin to OD_{600} of 0.8-1.0 and induction was initiated with 0.5 mM isopropyl-β-D-thiogalactopyranoside (IPTG) at 18 °C for 16 h. Cells were harvested at 4 °C by centrifugation and lysed in lysis buffer (40 mM Tris-HCl, 200 mM NaCl, 10% glycerol, 2 mM EDTA, 2 mM DTT, 0.1 mM PMSF, PH 8.0). Membranes were isolated from disrupted cells and solubilized with 2% n-dodecyl-β-D-maltopyranoside (DDM) in membrane solubilization buffer (40 mM Tris-HCl, 200 mM NaCl, 10% glycerol, 0.5 mM DTT, 0.1 mM PMSF, pH 8.0). The proteins were then purified by affinity chromatography on a Ni^{2+}-NTA column (Qiagen, Germany), washed with buffer containing 50 mM imidazole, 40 mM Tris-HCl (pH 8.0), 200 mM NaCl, 5% glycerol, 0.5 mM DTT, and 0.05% DDM, and eluted with buffer containing 300 mM imidazole, 40 mM Tris-HCl (pH 8.0), 200 mM NaCl, 5% glycerol, 0.5 mM DTT, and 0.05% DDM. Purified DddT was fractionated by gel filtration on a Superdex-200 column (GE Healthcare, USA) in buffer containing 20 mM Tris-HCl (pH 8.0), 200 mM NaCl, and 0.02% DDM.

Na^+/DMSP stoichiometry assay using solid-supported membrane (SSM) electrophysiology

Proteoliposomes were prepared by dissolving *E. coli* total lipid extract (12.5 mg/mL) in chloroform, drying under nitrogen, lyophilizing for 6 h, and resuspending in the appropriate B buffer (30 mM HEPES, 2 mM $MgCl_2$, 50 mM KCl, 50 mM NaCl, pH 7.5) supplemented with 40 mM DDM. Lipids were solubilized overnight at 4 °C with gentle agitation. The purified protein was exchanged into the same B buffer, then mixed with purified protein to achieve final concentrations of 4 mg/mL lipid and 0.8 mg/mL protein. Empty liposomes were prepared in parallel using identical lipid and buffer compositions without protein. Detergent was removed using Bio-Beads SM-2 overnight at 4 °C, yielding vesicle suspension.

Three independent proteoliposome batches were generated corresponding to B buffers B1, B2, and B3, containing 100, 200, and 50 μM DMSP, respectively. Empty liposomes were prepared in parallel in the same buffers. Proteoliposomes were sonicated using a bath sonicator (JP-010, Skymen, China) for 10 s, repeated three times, prior to use. Electrophysiological recordings were performed using a SURFE^{2}R N1 solid-supported membrane-based electrophysiology system (Nanion Technologies). N1 Single Sensors (Nanion Technologies; catalog no. 2-03-35002-000) were incubated with 50 μL of 0.5 mM 1-octadecanethiol in isopropanol for 30 min at room temperature. Sensors were washed twice with isopropanol, rinsed three times with distilled water, and air-dried. Subsequently, 1.5 μL of 7.5 μg/μL 1,2-diphytanoyl-sn-glycero-3-phosphocholine in n-decane was applied, followed by the addition of 50 μL of B buffer. Proteoliposomes (10 μL) were then applied to the sensors, which were centrifuged at 2000× *g* for 30 min at 25 °C to promote adsorption of the proteoliposomes onto the sensor surface. Transport currents were recorded using the B + BAB protocol, in which each sensor was perfused with the corresponding B buffer prior to each measurement, followed by rapid application of the paired A buffer (30 mM HEPES, 2 mM $MgCl_2$, 100 mM NaCl, and

50 or 200 µM DMSP), and subsequently re-perfused with the corresponding B buffer before the next measurement. Measurements were performed in triplicate.

Peak currents were normalized to the signals recorded from empty-liposome sensors under identical buffer-switch conditions to correct for non-specific capacitive contributions. Current amplitudes were plotted against the calculated chemical potential ratio $\Delta\mu(DMSP)/\Delta\mu(Na^+)$, yielding three data points corresponding to −1, −2, and +2 for B1/A1, B2/A2, and B3/A3 pairs, respectively. Linear regression of normalized peak currents versus chemical potential ratio was used to determine the apparent Na^+/DMSP coupling stoichiometry.

Cryo-EM sample preparation and data collection

The purified DddT protein samples were concentrated at 4 °C to 5 mg/mL in 20 mM Tris-HCl (pH 8.0), 200 mM NaCl/KCl, and 0.02% DDM. A 4.0-µL aliquot of the samples was applied onto a freshly glow-discharged holey carbon grid (Quantifoil Au R2/1, 200 mesh) with a continuous carbon support. The grids were plunge frozen in liquid ethane using an FEI Vitrobot Mark IV (Thermo-Fisher Scientific) at 4 °C and >90% humidity with 2 s blot time and −1 blot force. The grids were loaded into a 300 kV Titan Krios G3i microscope (Thermo Fisher) equipped with a K3 BioQuantum direct electron detector (Gatan, USA) for data acquisition. A total of 5747 movies for C_c was collected at a total dose for a stack of ~64 e^- $Å^{-2}$ in a defocus range of −1.6 to 2.2 µm. A total of 4845 movies for C_cS, 6804 movies for C_c-K^+, 4587 movies for C_e, and 6,174 movies for C_i were collected at a total dose for a stack of ~60 e^- $Å^{-2}$ in a defocus range of −0.8 to 1.6 µm. For C_c, a super-resolution mode was used at a nominal magnification of ×81,000 corresponding to a pixel size of 0.53 Å. For C_cS, C_c-K^+, C_e, and C_i, a super-resolution mode was used at a nominal magnification of ×130,000 corresponding to a pixel size of 0.97 Å.

Cryo-EM image processing

Data processing was performed using cryoSPARC Software (Punjani et al, 2017). After patch-motion and CTF correction were performed, particles were picked using the Blob picking algorithm of cryoSPARC. The particles were then subjected to several rounds of 2D classification. These runs yielded particles for analysis that were subjected to ab initio reconstructions. After homogeneous refinement and 3D non-uniform refinement, global (per-group) CTF refinement, and local (per-particle) CTF refinement were performed. The resolution was estimated using the gold standard Fourier shell correlation (FSC) of the 0.143 criteria in cryoSPARC. The overall resolutions of the maps of C_c, C_cS, C_c-K^+, C_e, and C_i were 2.8, 2.52, 3.18, 2.66, and 3.29 Å, respectively. Details of the cryo-EM data processing and associated parameters are provided in Appendix Table S1, Appendix Figs. S6, S8, S10, S13, and S15.

Model building and refinement

AlphaFold2 was initially used to predict DddT structure. It was then docked into the resolution cryo-EM map using UCSF Chimera (Pettersen et al, 2004). The DddT model in the C_c state was manually rebuilt based on the cryo-EM density using COOT (Casañal et al, 2020) and then refined using Phenix 1.16.3549 (Liebschner et al, 2019). The atomic model of DddT in the C_cS, C_c-K^+, C_e, and Ci states was built using a method similar to that of DddT, but using DddT as a reference starting model. The geometrical restraint of DMSP was generated from the Grade Web Server. MolProbity 4 (Williams et al, 2018) was used to evaluate the structure geometries. Images were rendered using Chimera and ChimeraX (Pettersen et al, 2021).

Bioinformatics

Using the representative bacterial genomes obtained from GenBank, homologues of DddT, DddD, and DddX were first identified by setting the E-value to $<1E^{-50}$ and similarity to >35% compared to functional DddT (*P.* sp. D2) (this study) and DddX (*P.* sp. D2) (Li et al, 2021), and DddD (*Marinomonas* sp. MWYL1) (Todd et al, 2007) using blastp. DddD homologues were further screened based on protein sequence length, retaining only those with sequences exceeding 600 amino acids. Subsequently, the genomic positions of genes corresponding to the selected protein homologues were analyzed. Only the protein sequences corresponding to *dddT* genes that were less than five genes away from *dddD*/*dddX* genes were retained. Finally, 61 putative DddT proteins clustered with DMSP cleavage enzymes DddD or DddX were obtained.

For metagenomic analysis, a hidden Markov model (HMM) was constructed using two functional DddT sequences obtained from *P.* sp. D2 and *H.* sp. HTNK1. This model was subsequently employed to search for DddT homologues from sediment samples (https://img.jgi.doe.gov/cgi-bin/m/main.cgi) and polar ocean samples (NCBI BioProject accession no. PRJNA588686), and Tara Ocean samples (https://tara-oceans.mio.osupytheas.fr/ocean-gene-atlas/). Hmmsearch (http://hmmer.org) was performed with a cut-off value of $<1E^{-50}$, a percentage identity >35%, and a sequence criterion of >400 amino acids. Phylogenetic trees were constructed using the maximum likelihood method in MEGA, version 7.0. Sequence alignment was performed using the BioEdit Sequence Alignment Editor with the ClustalW Multiple Alignment method. Visualization of the geographical and species distribution was performed using R software.

Data availability

The atomic coordinates and cryo-EM maps in this study for the DddT in closed substrate-free conformation (PDB entry 21FF; EMD-67623), DddT in closed DMSP-bound conformation (PDB entry 21FI; EMD-67626), DddT in closed substrate-free conformation in the presence of potassium ions and dimethylsulfoniopropionate (PDB entry 21FJ; EMD-67627), DddT G101D in substrate-free outward open conformation (PDB entry 21FH; EMD-67625), and DddT G101D in substrate-free inward open conformation (PDB entry 21FK; EMD-67628) have been deposited in the Protein Data Bank (http://www.rcsb.org) and the Electron Microscopy Data Bank (https://www.ebi.ac.uk/pdbe/emdb/).

The source data of this paper are collected in the following database record: biostudies:S-SCDT-10_1038-S44318-026-00798-w.

Expanded view data, supplementary information, appendices are available for this paper at https://doi.org/10.1038/s44318-026-00798-w.

Peer review information

A peer review file is available at https://doi.org/10.1038/s44318-026-00798-w

References

Alamo DD, Meiler J, Mchaourab HS (2022) Principles of alternating access in LeuT-fold transporters: commonalities and divergences. J Mol Biol 434:167746

Archer SD, Widdicombe CE, Tarran GA, Rees AP, Burkill PH (2001) Production and turnover of particulate dimethylsulphoniopropionate during a coccolithophore bloom in the northern North Sea. Aquat Micro Ecol 24:225–241

Belviso S, Buat-Ménard P, Putaud J-P, Nguyen BC, Claustre H, Neveux J (1993) Size distribution of dimethylsulfoniopropionate (DMSP) in areas of the tropical northeastern Atlantic Ocean and the Mediterranean Sea. Mar Chem 44:55–71

Broy S, Chen C, Hoffmann T, Brock NL, Nau-Wagner G, Jebbar M, Smits SHJ, Dickschat JS, Bremer E (2015) Abiotic stress protection by ecologically abundant dimethylsulfoniopropionate and its natural and synthetic derivatives: insights from *Bacillus subtilis*. Environ Microbiol 17:2362–2378

Bullock HA, Luo H, Whitman WB (2017) Evolution of dimethylsulfoniopropionate metabolism in marine phytoplankton and bacteria. Front Microbiol 8:637

Carrión O, Zhu X-Y, Williams BT, Wang J, Zhang X-H, Todd JD (2023) Molecular discoveries in microbial DMSP synthesis. Adv Micro Physiol 83:59–116

Casañal A, Lohkamp B, Emsley P (2020) Current developments in Coot for macromolecular model building of electron cryo-microscopy and crystallographic data. Protein Sci 29:1069–1078

Chen C, Beattie GA (2008) *Pseudomonas syringae* BetT is a low-affinity choline transporter that is responsible for superior osmoprotection by choline over glycine betaine. J Bacteriol 190:2717–2725

Coleman JA, Green EM, Gouaux E (2016) X-ray structures and mechanism of the human serotonin transporter. Nature 532:334–339

Cosquer A, Pichereau V, Pocard J-A, Minet J, Cormier M, Bernard T (1999) Nanomolar levels of dimethylsulfoniopropionate, dimethylsulfonioacetate, and glycine betaine are sufficient to confer osmoprotection to *Escherichia coli*. Appl Environ Microbiol 65:3304–3311

Curson ARJ, Sullivan MJ, Todd JD, Johnston AWB (2010) Identification of genes for dimethyl sulfide production in bacteria in the gut of Atlantic herring (*Clupea harengus*). ISME J 4:144–146

Curson ARJ, Todd JD, Sullivan MJ, Johnston AWB (2011) Catabolism of dimethylsulphoniopropionate: microorganisms, enzymes and genes. Nat Rev Microbiol 9:849–859

Dehio C, Meyer M (1997) Maintenance of broad-host-range incompatibility group P and group Q plasmids and transposition of Tn5 in *Bartonella henselae* following conjugal plasmid transfer from *Escherichia coli*. J Bacteriol 179:538–540

Faham S, Watanabe A, Besserer GM, Cascio D, Specht A, Hirayama BA, Wright EM, Abramson J (2008) The crystal structure of a sodium galactose transporter reveals mechanistic insights into Na^+/sugar symport. Science 321:810–814

Galí M, Devred E, Levasseur M, Royer S-J, Babin M (2015) A remote sensing algorithm for planktonic dimethylsulfoniopropionate (DMSP) and an analysis of global patterns. Remote Sens Environ 171:171–184

Gao C, Fernandez VI, Lee KS, Fenizia S, Pohnert G, Seymour JR, Raina J-B, Stocker R (2020) Single-cell bacterial transcription measurements reveal the importance of dimethylsulfoniopropionate (DMSP) hotspots in ocean sulfur cycling. Nat Commun 11:1942

Gregory GJ, Boas KE, Boyd EF (2021) The organosulfur compound dimethylsulfoniopropionate (DMSP) is utilized as an osmoprotectant by *Vibrio* species. Appl Environ Microbiol 87:e02235–02220

Güell-Bujons Q, Zanoli M, Tuval I, Calbet A, Simó R (2024) Distinctive chemotactic responses of three marine herbivore protists to DMSP and related compounds. ISME J 18:ware130

Heuchert A, Glöckner FO, Amann R, Fischer U (2004) *Psychrobacter nivimaris* sp. nov., a heterotrophic bacterium attached to organic particles isolated from the South Atlantic (Antarctica). Syst Appl Microbiol 27:399–406

Hopkins FE, Archer SD, Bell TG, Suntharalingam P, Todd JD (2023) The biogeochemistry of marine dimethylsulfide. Nat Rev Earth Environ 4:361–376

Kalayil S, Schulze S, Kühlbrandt W (2013) Arginine oscillation explains Na^+ independence in the substrate/product antiporter CaiT. Proc Natl Acad Sci USA 110:17296–17301

Katsuhiro N, Sato K, Takase R, Kawai S, Ogura K, Hashimoto W (2024) Decomposition of brown algae in the ocean by microbiota: biological insights for recycling blue carbon. Biosci Biotechnol Biochem 88:1487–1495

Khafizov K, Perez C, Koshy C, Quick M, Fendler K, Ziegler C, Forrest LR (2012) Investigation of the sodium-binding sites in the sodium-coupled betaine transporter BetP. Proc Natl Acad Sci USA 109:E3035–E3044

Kiene RP, Linn LJ, Bruton JA (2000) New and important roles for DMSP in marine microbial communities. J Sea Res 43:209–224

Kiene RP, Nowinski B, Esson K, Preston C, Marin IIIR, Birch J, Scholin C, Ryan J, Moran MA (2019) Unprecedented DMSP concentrations in a massive dinoflagellate bloom in Monterey Bay, CA. Geophys Res Lett 46:12279–12288

Kovach ME, Elzer PH, Hill DS, Robertson GT, Farris MA, Roop 2ndRM, Peterson KM (1995) Four new derivatives of the broad-host-range cloning vector pBBR1MCS, carrying different antibiotic-resistance cassettes. Gene 166:175–176

Krämer R, Morbach S (2004) BetP of *Corynebacterium glutamicum*, a transporter with three different functions: betaine transport, osmosensing, and osmoregulation. Biochim Biophys Acta 1658:31–36

Krishnamurthy H, Gouaux E (2012) X-ray structures of LeuT in substrate-free outward-open and apo inward-open states. Nature 481:469–474

Li C-Y, Mausz MA, Murphy A, Zhang N, Chen X-L, Wang S-Y, Gao C, Aguilo-Ferretjans MM, Silvano E, Lidbury IDEA et al (2023) Ubiquitous occurrence of a dimethylsulfoniopropionate ABC transporter in abundant marine bacteria. ISME J 17:579–587

Li C-Y, Wang X-J, Chen X-L, Sheng Q, Zhang S, Wang P, Quareshy M, Rihtman B, Shao X, Gao C et al (2021) A novel ATP dependent dimethylsulfoniopropionate lyase in bacteria that releases dimethyl sulfide and acryloyl-CoA. eLife 10:e64045

Liebschner D, Afonine PV, Baker ML, Bunkóczi G, Chen VB, Croll TI, Hintze B, Hung L-W, Jain S, McCoy AJ et al (2019) Macromolecular structure determination using X-rays, neutrons and electrons: recent developments in Phenix. Acta Crystallogr D Struct Biol 75:861–877

Liu J, Liu J, Zhang S-H, Liang J, Lin H, Song D, Yang G-P, Todd JD, Zhang X-H (2018) Novel insights into bacterial dimethylsulfoniopropionate catabolism in the East China Sea. Front Microbiol 9:3206

Malinauskaite L, Quick M, Reinhard L, Lyons JA, Yano H, Javitch JA, Nissen P (2014) A mechanism for intracellular release of Na^+ by neurotransmitter/sodium symporters. Nat Struct Mol Biol 21:1006–1012

Mungall EL, Croft B, Lizotte M, Thomas JL, Murphy JG, Levasseur M, Martin RV, Wentzell JJB, Liggio J, Abbatt JPD (2016) Dimethyl sulfide in the summertime Arctic atmosphere: measurements and source sensitivity simulations. Atmos Chem Phys 16:6665–6680

Perez C, Faust B, Mehdipour AR, Francesconi KA, Forrest LR, Ziegler C (2014) Substrate-bound outward-open state of the betaine transporter BetP provides insights into Na^+ coupling. Nat Commun 5:4231

Perez C, Koshy C, Yildiz Ö, Ziegler C (2012) Alternating-access mechanism in conformationally asymmetric trimers of the betaine transporter BetP. Nature 490:126–130

Pettersen EF, Goddard TD, Huang CC, Couch GS, Greenblatt DM, Meng EC, Ferrin TE (2004) UCSF Chimera—a visualization system for exploratory research and analysis. J Comput Chem 25:1605–1612

Pettersen EF, Goddard TD, Huang CC, Meng EC, Couch GS, Croll TI, Morris JH, Ferrin TE (2021) UCSF ChimeraX: structure visualization for researchers, educators, and developers. Protein Sci 30:70–82

Punjani A, Rubinstein JL, Fleet DJ, Brubaker MA (2017) cryoSPARC: algorithms for rapid unsupervised cryo-EM structure determination. Nat Methods 14:290–296

Reisch CR, Moran MA, Whitman WB (2008) Dimethylsulfoniopropionate-dependent demethylase (DmdA) from *Pelagibacter ubique* and *Silicibacter pomeroyi*. J Bacteriol 190:8018–8024

Reisch CR, Moran MA, Whitman WB (2011) Bacterial catabolism of dimethylsulfoniopropionate (DMSP). Front Microbiol 2:172

Ressl S, Scheltinga ACTV, Vonrhein C, Ott V, Ziegler C (2009) Molecular basis of transport and regulation in the Na^+/betaine symporter BetP. Nature 458:47–52

Schulze S, Köster S, Geldmacher U, Scheltinga ACTV, Kühlbrandt W (2010) Structural basis of Na^+-independent and cooperative substrate/product antiport in CaiT. Nature 467:233–236

Shahsavar A, Stohler P, Bourenkov G, Zimmermann I, Siegrist M, Guba W, Pinard E, Sinning S, Seeger MA, Schneider TR et al (2021) Structural insights into the inhibition of glycine reuptake. Nature 591:677–681

Shaw DK, Sekar J, Ramalingam PV (2022) Recent insights into oceanic dimethylsulfoniopropionate biosynthesis and catabolism. Environ Microbiol 24:2669–2700

Simó R, Archer SD, Pedrós-Alió C, Gilpin L, Stelfox-Widdicombe CE (2002) Coupled dynamics of dimethylsulfoniopropionate and dimethylsulfide cycling and the microbial food web in surface waters of the North Atlantic. Limnol Oceanogr 47:53–61

Stefels J (2000) Physiological aspects of the production and conversion of DMSP in marine algae and higher plants. J Sea Res 43:183–197

Sun J, Todd JD, Thrash JC, Qian Y, Qian MC, Temperton B, Guo J, Fowler EK, Aldrich JT, Nicora CD et al (2016) The abundant marine bacterium *Pelagibacter* simultaneously catabolizes dimethylsulfoniopropionate to the gases dimethyl sulfide and methanethiol. Nat Microbiol 1:16065

Sun L, Curson ARJ, Todd JD, Johnston AWB (2012) Diversity of DMSP transport in marine bacteria, revealed by genetic analyses. Biogeochemistry 110:121–130

Sunda W, Kieber DJ, Kiene RP, Huntsman S (2002) An antioxidant function for DMSP and DMS in marine algae. Nature 418:317–320

Tang L, Bai L, Wang WH, Jiang T (2010) Crystal structure of the carnitine transporter and insights into the antiport mechanism. Nat Struct Mol Biol 17:492–496

Taylor BF, Gilchrist DC (1991) New routes for aerobic biodegradation of dimethylsulfoniopropionate. Appl Environ Microbiol 57:3581–3584

Teng Z-J, Qin Q-L, Zhang W, Li J, Fu H-H, Wang P, Lan M, Luo G, He J, McMinn A et al (2021) Biogeographic traits of dimethyl sulfide and dimethylsulfoniopropionate cycling in polar oceans. Microbiome 9:207

Todd JD, Curson ARJ, Nikolaidou-Katsaraidou N, Brearley CA, Watmough NJ, Chan Y, Page PCB, Sun L, Johnston AWB (2010) Molecular dissection of bacterial acrylate catabolism-unexpected links with dimethylsulfoniopropionate catabolism and dimethyl sulfide production. Environ Microbiol 12:327–343

Todd JD, Rogers R, Li YG, Wexler M, Bond PL, Sun L, Curson ARJ, Malin G, Steinke M, Johnston AWB (2007) Structural and regulatory genes required to make the gas dimethyl sulfide in bacteria. Science 315:666–669

Veres PR, Neuman JA, Bertram TH, Assaf E, Wolfe GM, Williamson CJ, Weinzierl B, Tilmes S, Thompson CR, Thames AB et al (2020) Global airborne sampling reveals a previously unobserved dimethyl sulfide oxidation mechanism in the marine atmosphere. Proc Natl Acad Sci USA 117:4505–4510

Wahlgren WY, Dunevall E, North RA, Paz A, Scalise M, Bisignano P, Bengtsson-Palme J, Goyal P, Claesson E, Caing-Carlsson R et al (2018) Substrate-bound outward-open structure of a Na^+-coupled sialic acid symporter reveals a new Na^+ site. Nat Commun 9:1753

Wang KH, Penmatsa A, Gouaux E (2015a) Neurotransmitter and psychostimulant recognition by the dopamine transporter. Nature 521:322–327

Wang P, Chen X-L, Li C-Y, Gao X, Zhu D-Y, Xie B-B, Qin Q-L, Zhang X-Y, Su H-N, Zhou B-C et al (2015b) Structural and molecular basis for the novel catalytic mechanism and evolution of DddP, an abundant peptidase-like bacterial dimethylsulfoniopropionate lyase: a new enzyme from an old fold. Mol Microbiol 98:289–301

Weyand S, Shimamura T, Yajima S, Suzuki SI, Mirza O, Krusong K, Carpenter EP, Rutherford NG, Hadden JM, O'Reilly J et al (2008) Structure and molecular mechanism of a nucleobase-cation-symport-1 family transporter. Science 322:709–713

Williams CJ, Headd JJ, Moriarty NW, Prisant MG, Videau LL, Deis LN, Verma V, Keedy DA, Hintze BJ, Chen VB et al (2018) MolProbity: more and better reference data for improved all-atom structure validation. Protein Sci 27:293–315

Wirth JS, Wang T, Huang Q, White RH, Whitman WB (2020) Dimethylsulfoniopropionate sulfur and methyl carbon assimilation in *Ruegeria* species. mBio 11:e00329–00320

Yamashita A, Singh SK, Kawate T, Jin Y, Gouaux E (2005) Crystal structure of a bacterial homologue of Na^+/Cl^--dependent neurotransmitter transporters. Nature 437:215–223

Yoch DC (2002) Dimethylsulfoniopropionate: its sources, role in the marine food web, and biological degradation to dimethylsulfide. Appl Environ Microbiol 68:5804–5815

Yoch DC, Ansede JH, Rabinowitz KS (1997) Evidence for intracellular and extracellular dimethylsulfoniopropionate (DMSP) lyases and DMSP uptake sites in two species of marine bacteria. Appl Environ Microbiol 63:3182–3188

Zhang X-H, Liu J, Liu J, Yang G, Xue C-X, Curson ARJ, Todd JD (2019) Biogenic production of DMSP and its degradation to DMS-their roles in the global sulfur cycle. Sci China Life Sci 62:1296–1319

Zheng Y, Wang J, Zhou S, Zhang Y, Liu J, Xue C-X, Williams BT, Zhao X, Zhao L, Zhu X-Y et al (2020) Bacteria are important dimethylsulfoniopropionate producers in marine aphotic and high-pressure environments. Nat Commun 11:4658

Ziegler C, Bremer E, Krämer R (2010) The BCCT family of carriers: from physiology to crystal structure. Mol Microbiol 78:13–34

Acknowledgements

We are grateful to Dr. Qiu-Yao Jiang (Shandong First Medical University, China) for cryo-EM data collection. We thank Dr. Xiao-Ju Li (State Key Laboratory of Microbial Technology, Shandong University) for their assistance with TEM. We thank Prof. Guanghua Huang and Dr. Jian Bing for their assistance with solid-supported membrane (SSM) electrophysiology assays. This work was funded by the National Natural Science Foundation of China (32330001, W2441012, 32170127, 32370136), the National Key R&D Program of China (2024YFC2816000), Program of Shandong for Taishan Scholars (tspd20240806 and tsqn202408064), Shandong Province Science Fund for Excellent Young Scholars (ZR2025QB18), Biotechnology and Biological Sciences Research Council (BB/Y01135X/1), Natural Environment Research Council (NE/Z00019X/1) and the SKLMT Frontiers and Challenges Project (SKLMTFCP-2023-06).

Author contributions

Yu-Zhong Zhang: Funding acquisition; Validation; Investigation; Project administration; Writing—review and editing. **Wen-Jing Zhu**: Data curation; Formal analysis; Validation; Investigation; Writing—original draft. **Kang Li**: Investigation; Methodology. **Hai-Tao Ding**: Investigation; Methodology. **Motoyuki Hattori**: Formal analysis; Validation; Methodology. **Shuaimeng Liu**: Investigation; Methodology. **Chang Ge**: Data curation; Investigation. **Qi-Long Qin**: Data curation; Investigation; Methodology. **Zhao-Jie Teng**: Data curation; Methodology. **Ning-Hua Liu**: Data curation; Methodology. **Hai-Yan Cao**: Investigation; Methodology. **Chun-Yang Li**: Data curation; Methodology. **Xiu-Lan Chen**: Formal analysis; Methodology; Writing—review and editing. **Qing-Tao Shen**: Methodology; Writing—review and editing. **Jonathan D Todd**: Formal analysis; Methodology; Writing—review and editing. **Lu-Ning Liu**: Funding acquisition; Validation; Methodology; Writing—review and editing. **Peng Wang**: Conceptualization; Funding acquisition; Validation; Investigation; Methodology; Writing—original draft; Project administration; Writing—review and editing.

Source data underlying figure panels in this paper may have individual authorship assigned. Where available, figure panel/source data authorship is listed in the following database record: biostudies:S-SCDT-10_1038-S44318-026-00798-w.

Disclosure and competing interests statement

The authors declare no competing interests.

Expanded View Figures

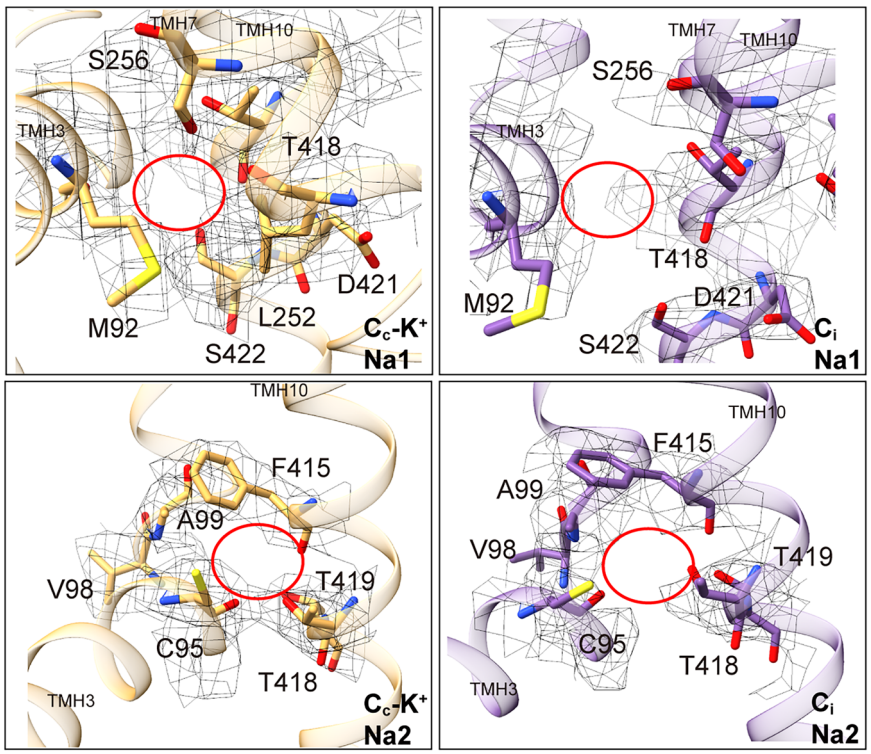

Figure EV1. Loss of cryo-EM densities at the putative Na1 and Na2 sites in the C_c-K^+ and C_i structures determined in Na^+-free buffer.

The gray mesh shows the local cryo-EM density of the residues involved in sodium binding, contoured at 4 RMSD. The densities corresponding to Na1 and Na2, which are clearly observed in the C_e and C_cS states, are absent under Na^+-free conditions.

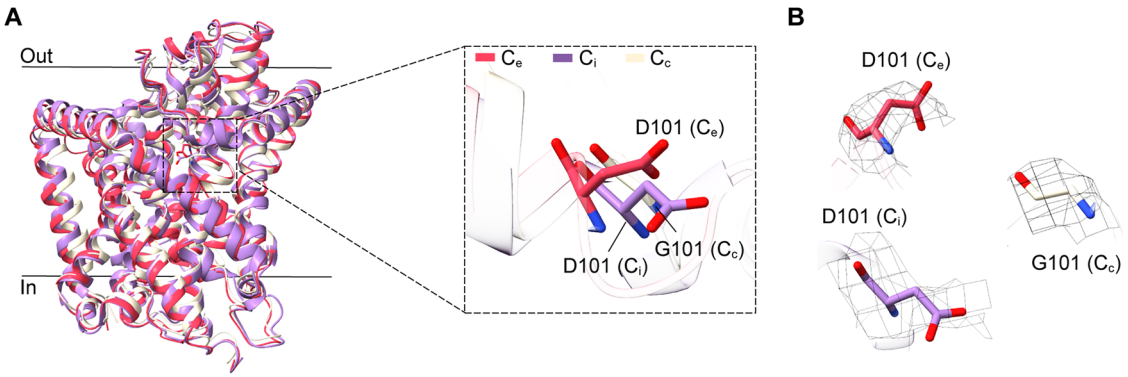

Figure EV2. Structural comparison of residue 101 in DddT among the C_c, C_e, and C_i states.

(**A**) Structural differences of residue 101 between the C_c, C_e, and C_i states. The C_c, C_e, and C_i states are colored in beige, red, and purple, respectively. (**B**) Cryo-EM densities surrounding Asp101 (C_e), Asp101 (C_i), and Gly101 (C_c), contoured at 6 RMSD, 4 RMSD, and 8 RMSD, respectively.

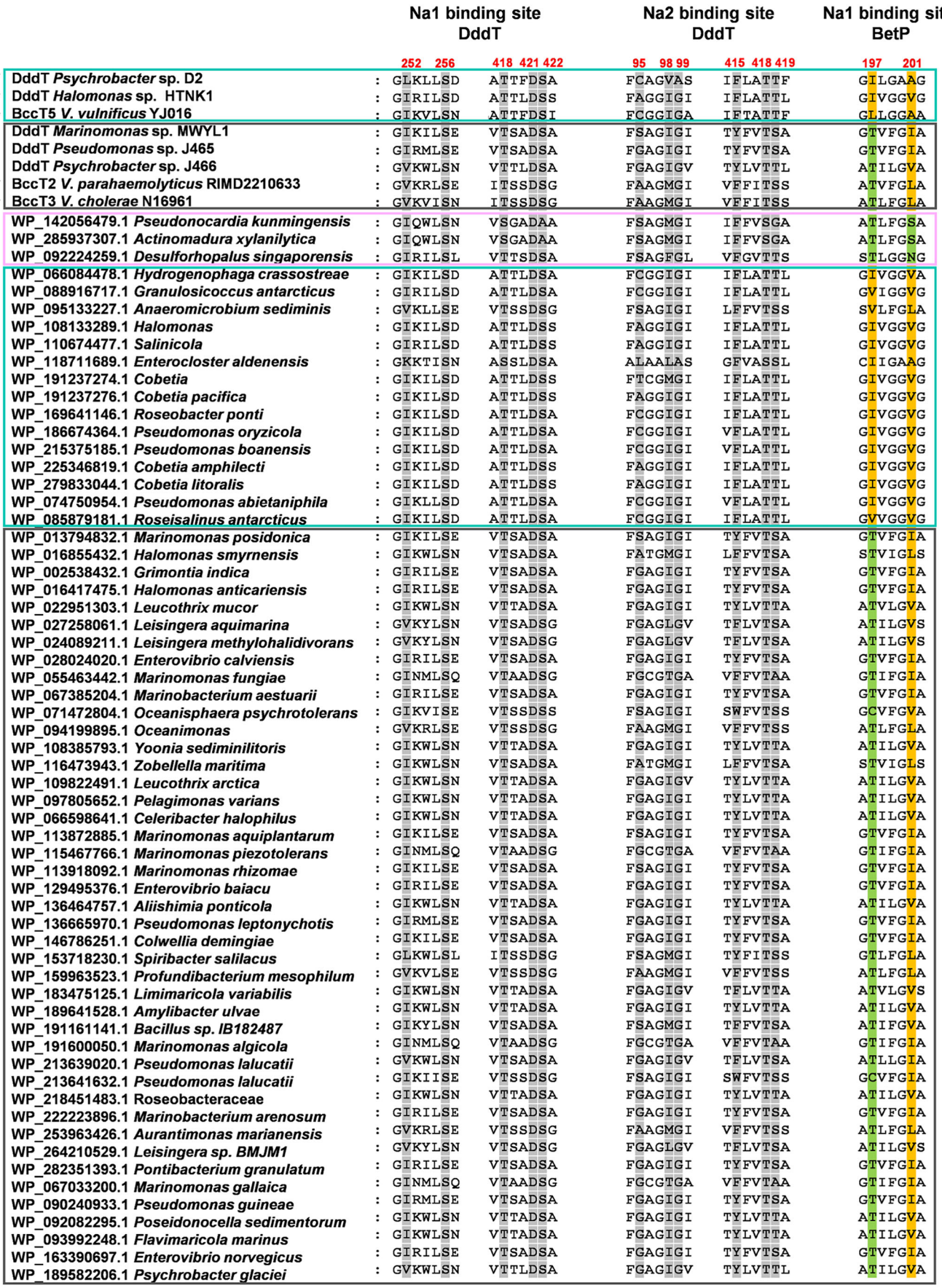
Na1 binding site DddT
Na2 binding site DddT
Na1 binding site BetP
252 256 418 421 422 95 98 99 415 418 419 197 201
★ DddT Psychrobacter sp. D2 : GLKLLSD ATTFDSA FCAGVAS IFLATTF GILGAAG
★ DddT Halomonas sp. HTNK1 : GIRILSD ATTLDSS FAGGIGI IFLATTL GIVGGVG
★ BccT5 V. vulnificus YJ016 : GIKVLSN ATTFDSI FCGGIGA IFTATTF GLLGGAA
DddT Marinomonas sp. MWYL1 : GIKILSE VTSADSA FSAGIGI TYFVTSA GTVFGIA
DddT Pseudomonas sp. J465 : GIRMLSE VTSADSA FGAGIGI TYFVTSA GTVFGIA
DddT Psychrobacter sp. J466 : GVKWLSN VTTLDSA FGAGIGV TYLVTTL ATILGVA
★ BccT2 V. parahaemolyticus RIMD2210633 : GVKRLSE ITSSDSG FAAGMGI VFFITSS ATVFGLA
★ BccT3 V. cholerae N16961 : GVKVISN ITSSDSG FAAGMGI VFFITSS ATLFGLA
WP_142056479.1 Pseudonocardia kunmingensis : GIQWLSN VSGADAA FSAGMGI IFFVSGA ATLFGSA
WP_285937307.1 Actinomadura xylanilytica : GIQWLSN VSGADAA FSAGMGI IFFVSGA ATLFGSA
WP_092224259.1 Desulforhopalus singaporensis : GIRILSL VTTSDSA FSAGFGL VFGVTTS STLGGNG
WP_066084478.1 Hydrogenophaga crassostreae : GIKILSD ATTLDSA FCGGIGI IFLATTL GIVGGVA
WP_088916717.1 Granulosicoccus antarcticus : GIRILSD ATTLDSA FCGGIGI IFLATTL GVIGGVG
WP_095133227.1 Anaeromicrobium sediminis : GVKLLSE VTSSDSG FSAGIGI LFFVTSS SVLFGLA
WP_108133289.1 Halomonas : GIKILSD ATTLDSS FAGGIGI IFLATTL GIVGGVG
WP_110674477.1 Salinicola : GIRILSD ATTLDSS FAGGIGI IFLATTL GIVGGVG
WP_118711689.1 Enterocloster aldenensis : GKKTISN ASSLDSA ALAALAS GFVASSL CIIGAAG
WP_191237274.1 Cobetia : GIKILSD ATTLDSS FTCGMGI IFLATTL GIVGGVG
WP_191237276.1 Cobetia pacifica : GIKILSD ATTLDSS FAGGIGI IFLATTL GIVGGVG
WP_169641146.1 Roseobacter ponti : GIKILSD ATTLDSA FCGGIGI IFLATTL GIVGGVG
WP_186674364.1 Pseudomonas oryzicola : GIKILSD ATTLDSA FCGGIGI VFLATTL GIVGGVG
WP_215375185.1 Pseudomonas boanensis : GIKILSD ATTLDSA FCGGIGI VFLATTL GIVGGVG
WP_225346819.1 Cobetia amphilecti : GIKILSD ATTLDSS FAGGIGI IFLATTL GIVGGVG
WP_279833044.1 Cobetia litoralis : GIKILSD ATTLDSS FAGGIGI IFLATTL GIVGGVG
WP_074750954.1 Pseudomonas abietaniphila : GIKLLSD ATTLDSA FCGGIGI VFLATTL GIVGGVG
WP_085879181.1 Roseisalinus antarcticus : GIKILSD ATTLDSA FCGGIGI IFLATTL GVVGGVG
WP_013794832.1 Marinomonas posidonica : GIKILSE VTSADSA FSAGIGI TYFVTSA GTVFGIA
WP_016855432.1 Halomonas smyrnensis : GIKWLSN VTSADSA FATGMGI LFFVTSA STVIGLS
WP_002538432.1 Grimontia indica : GIRILSE VTSADSA FGAGIGI TYFVTSA GTVFGIA
WP_016417475.1 Halomonas anticariensis : GIRILSE VTSADSA FGAGIGI TYFVTSA GTVFGIA
WP_022951303.1 Leucothrix mucor : GIKWLSN VTTADSA FGAGIGI TYLVTTA ATVLGVA
WP_027258061.1 Leisingera aquimarina : GVKYLSN VTSADSG FGAGLGV TFLVTSA ATILGVS
WP_024089211.1 Leisingera methylohalidivorans : GVKYLSN VTSADSG FGAGLGV TFLVTSA ATILGVS
WP_028024020.1 Enterovibrio calviensis : GIRILSE VTSADSA FGAGIGI TYFVTSA GTVFGIA
WP_055463442.1 Marinomonas fungiae : GINMLSQ VTAADSG FGCGTGA VFFVTAA GTIFGIA
WP_067385204.1 Marinobacterium aestuarii : GIRILSE VTSADSA FGAGIGI TYFVTSA GTVFGIA
WP_071472804.1 Oceanisphaera psychrotolerans : GIKVISE VTSSDSS FSAGIGI SWFVTSS GCVFGVA
WP_094199895.1 Oceanimonas : GVKRLSE VTSSDSG FAAGMGI VFFVTSS ATLFGLA
WP_108385793.1 Yoonia sediminilitoris : GIKWLSN VTTADSA FGAGIGI TYLVTTA ATILGVA
WP_116473943.1 Zobellella maritima : GIKWLSN VTSADSA FATGMGI LFFVTSA STVIGLS
WP_109822491.1 Leucothrix arctica : GIKWLSN VTTADSA FGAGIGV TYLVTTA ATILGVA
WP_097805652.1 Pelagimonas varians : GIKWLSN VTTADSA FGAGIGI TYLVTTA ATILGVA
WP_066598641.1 Celeribacter halophilus : GIKWLSN VTTADSA FGAGIGI TYLVTTA ATILGVA
WP_113872885.1 Marinomonas aquiplantarum : GIKILSE VTSADSA FSAGIGI TYFVTSA GTVFGIA
WP_115467766.1 Marinomonas piezotolerans : GINMLSQ VTAADSG FGCGTGA VFFVTAA GTIFGIA
WP_113918092.1 Marinomonas rhizomae : GIKILSE VTSADSA FSAGIGI TYFVTSA GTVFGIA
WP_129495376.1 Enterovibrio baiacu : GIRILSE VTSADSA FGAGIGI TYFVTSA GTVFGIA
WP_136464757.1 Aliishimia ponticola : GIKWLSN VTTADSA FGAGIGI TYLVTTA ATILGVA
WP_136665970.1 Pseudomonas leptonychotis : GIRMLSE VTSADSA FGAGIGI TYFVTSA GTVFGIA
WP_146786251.1 Colwellia demingiae : GIKILSE VTSADSA FGAGIGI TYFVTSA GTVFGIA
WP_153718230.1 Spiribacter salilacus : GLKWLSL ITSSDSG FSAGMGI TYFITSS GTLFGLA
WP_159963523.1 Profundibacterium mesophilum : GVKVLSE VTSSDSG FAAGMGI VFFVTSS ATLFGLA
WP_183475125.1 Limimaricola variabilis : GIKWLSN VTTADSA FGAGIGV TFLVTTA ATVLGVS
WP_189641528.1 Amylibacter ulvae : GIKWLSN VTTADSA FGAGIGI TYLVTTA ATILGVA
WP_191161141.1 Bacillus sp. IB182487 : GIKYLSN VTSADSA FSAGMGI TFFVTSA ATIFGVA
WP_191600050.1 Marinomonas algicola : GINMLSQ VTAADSG FGCGTGA VFFVTAA GTIFGIA
WP_213639020.1 Pseudomonas lalucatii : GVKWLSN VTSADSA FGAGIGV TFLVTSA ATLLGIA
WP_213641632.1 Pseudomonas lalucatii : GIKIISE VTSSDSG FSAGIGI SWFVTSS GCVFGIA
WP_218451483.1 Roseobacteraceae : GIKWLSN VTTADSA FGAGIGI TYLVTTA ATILGVA
WP_222223896.1 Marinobacterium arenosum : GIRILSE VTSADSA FGAGIGI TYFVTSA GTVFGIA
WP_253963426.1 Aurantimonas marianensis : GVKRLSE VTSSDSG FAAGMGI VFFVTSS ATLFGLA
WP_264210529.1 Leisingera sp. BMJM1 : GVKYLSN VTSADSG FGAGLGV TFLVTSA ATILGVS
WP_282351393.1 Pontibacterium granulatum : GIRILSE VTSADSA FGAGIGI TYFVTSA GTVFGIA
WP_067033200.1 Marinomonas gallaica : GINMLSQ VTAADSG FGCGTGA VFFVTAA GTIFGIA
WP_090240933.1 Pseudomonas guineae : GIRMLSE VTSADSA FGAGIGI TYFVTSA GTVFGIA
WP_092082295.1 Poseidonocella sedimentorum : GIKWLSN VTTADSA FGAGIGI TYLVTTA ATILGVA
WP_093992248.1 Flavimaricola marinus : GIKWLSN VTTADSA FGAGIGI TYLVTTA ATILGVA
WP_163390697.1 Enterovibrio norvegicus : GIRILSE VTSADSA FGAGIGI TYFVTSA GTVFGIA
WP_189582206.1 Psychrobacter glaciei : GVKWLSN VTTLDSA FGAGIGV TYLVTTL ATILGVA

◀ **Figure EV3. Multi-sequence alignment of the experimentally ratified DddT proteins and 61 identified DddT homologues whose genes are linked to the DMSP lyase genes DddD/DddX.**

Key residues around the sodium-binding site are marked out. Based on the hydrophilicity and hydrophobicity of key residues at the Na1-binding site of BetP, sequences are divided into three categories. In the gray box, there is one hydrophilic residue and one hydrophobic residue. In the blue box, both residues are hydrophilic, and in the pink box, both residues are hydrophobic. The functional DddTs are marked with ★. Hydrophilic residues are colored green, and hydrophobic residues are colored orange. Source data are available online for this figure.

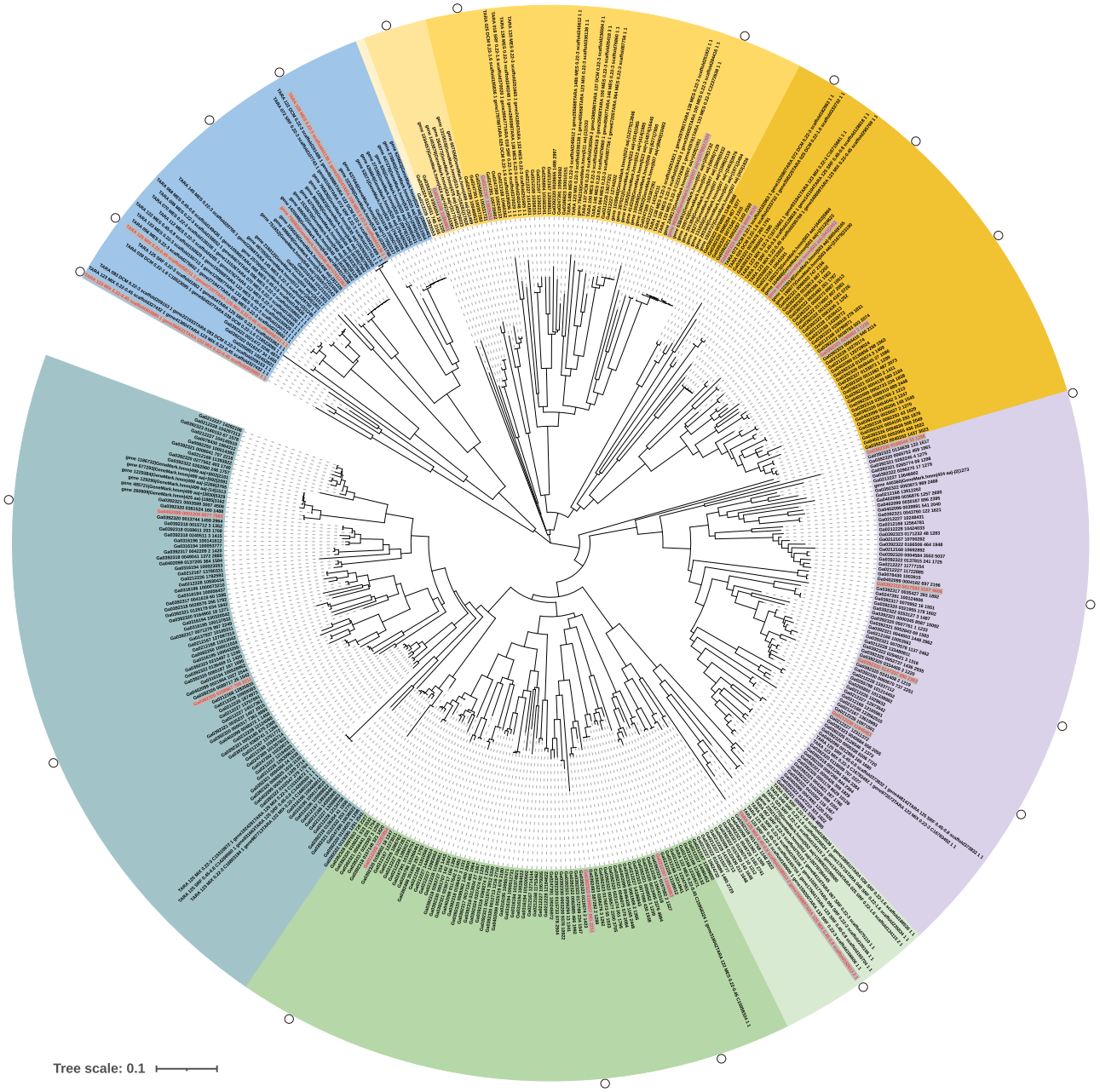

Figure EV4. Phylogenetic analysis of selected 411 DddT homologues from metagenome data.

Branches with different colors represent distinct clades in the phylogenetic tree. The sequences highlighted by shading and shown in red within the circle correspond to 20 randomly selected sequences from different branches of the phylogenetic tree, which were used for the multiple sequence alignment in Fig. 6C. Source data are available online for this figure.

